# 1 River body extraction from Sentinel-2A/B MSI images based on an adaptive

# 2 multi-scale region growth method

- 3 Song Jin<sup>a,b,c</sup>, Yongxue Liu<sup>a,b\*</sup>, Sergio Fagherazzi<sup>c</sup>, Huan Mi<sup>c,d</sup>, Gang Qiao<sup>d\*</sup>, Wenxuan Xu<sup>a,b</sup>, Chao
- 4 Sune, Yongchao Liu<sup>a,b</sup>, Bingxue Zhao<sup>a,b</sup>, Cédric G. Fichot<sup>c</sup>
- 5 <sup>a</sup> School of Geography and Ocean Science, Nanjing University, Nanjing, Jiangsu Province, 210046, P. R. China
- 6 b Key Laboratory of Coastal Zone Exploitation and Protection, Ministry of Natural Resources of China, Nanjing
- 7 University, Nanjing, 210023, China
- 9 d College of Surveying and Geo-Informatics, Tongji University, Shanghai 200092, China
- 10 <sup>e</sup> Department of Geography & Spatial Information Techniques, Ningbo University, Ningbo, Zhejiang Province
- 11 315211, PR China

- 12 The full name and details of the corresponding author:
- 13 Yongxue Liu, Ph. D, Professor, Nanjing University, Nanjing, Jiangsu Province, 210046, P. R. China. Email:
- 14 <u>yongxue@nju.edu.cn</u>. Tel/FAX: +86-25-89881181.
- 15 Gang Qiao, Ph. D, Professor, Tongji University, Shanghai, 200092, P. R. China. Email:
- 16 qiaogang@tongji.edu.cn
- 17 The full names and details of all co-authors of the paper:
- 18 Song Jin, Nanjing University, Nanjing, Jiangsu Province, 210046, P. R. China. Email:
- 19 jinsong nju@foxmail.com
- 20 Sergio Fagherazzi, Boston University, Boston, MA 02215, U.S.A. Email: sergio@bu.edu
- 21 Huan Mi, Tongji University, Shanghai, 200092, P. R. China. Email: 2015mihuan@tongji.edu.cn
- Wenxuan Xu, Nanjing University, Nanjing, Jiangsu Province, 210046, P. R. China. Email:
- wenxuan@smail.nju.edu.cn
- Chao Sun, Ningbo University, Ningbo, Zhejiang Province 315211, P. R. China. Email: sunchaonju@yeah.net
- 25 Yongchao Liu, Nanjing University, Nanjing, Jiangsu Province, 210046, P. R. China. Email:
- yongchaoliu@smail.nju.edu.cn
- 27 Bingxue Zhao, Nanjing University, Nanjing, Jiangsu Province, 210046, P. R. China. Email:
- bingxue@smail.nju.edu.cn
- 29 Cédric G.Fichot, Boston University, Boston, MA 02215, U.S.A. Email: cgfichot@bu.edu

# 30 Highlights:

- A method is proposed for extracting river networks from MSI images
- Background homogenization and adaptive multi-scale region growth are adopted
- The proposed method is sensitive to multiple scales of river networks
- The strategy of "fast-growing and fine-screening" is used

**Abstract:** River networks are important water carriers that provide a multitude of ecosystem services, including freshwater for agriculture, drinking water for cities, and recreational activities. Accurate mapping of river networks from remote-sensing images is important for the study of these systems. Unfortunately, the delineation of river networks is challenging due to the spatial variability of the river channels, the complexity of the surrounding landscape, and the multi-scale characteristics of the network. Here, we present an adaptive, multiscale region growth method (AMRGM) to delineate river networks from Sentinel-2A/B MSI images. The method can handle the variability of river surroundings, multiple spatial scales, and the variable curvature of the channels. The method includes four steps: (i) a water index (NDWI) is used to enhance river bodies information; (ii) a bias-corrected fuzzy C-means (BCFCM) method mitigates the heterogeneity of the background; (iii) a scale-enhancement algorithm based on the Hessian Matrix makes full use of scale and direction information, and (iv) a regional growth criterion handles various river dimensions. Fast-growing and fine-screening strategies are also included in the AMRGM. The method is applied to eight river networks to evaluate its accuracy and reliability with various river morphologies and climate conditions. The AMRGM presents several advantages for detecting multi-scale river branches compared to four commonly used river-detection methods (i.e., K-means method, maximum likelihood method, Iterative Self-Organizing Data Analysis Technique Algorithm, and Support Vector Machine). The mean overall accuracy (OA) and kappa coefficients (KC) of the AMRGM exceed 97% and 0.92 across the eight river networks. The most accurate river extractions are obtained for the Amazon River, Mackenzie River, and the Ganges Delta, where the river scale and direction characteristics are most distinct. Relatively high omission and commission errors are present in river networks displaying a complex and heterogeneous zonation, such as the River Welland, UK, and the Zagya Zangbo River in the Tibet Plateau. The complex geomorphic features of the River Welland reduce OA and KC to 93.8% and 0.86, respectively.

35

36

37

38

39

40

41

42

43

44

45

46

47

48

49

50

51

52

53

54

55

56

57

Keywords: Sentinel-2A/B MSI, AMRGM, Hessian Matrix, Fast-growing and fine-screening

#### 1. Introduction

Terrestrial rivers play an essential role in the global water cycle and provide water at the continental scale for irrigation, hydroelectricity, and urban needs (Bookhagen and Burbank 2010; Vörösmarty et al. 2003). As sea level rises and climate changes, river networks may dramatically change in morphology, affecting the delivery of water, sediments, and biologically important compounds to the Earth's surface. Biological and physical processes control the landscape surrounding rivers and the network morphology and multi-scale characteristics. Comprehensive and precise mapping of river channels is critical to understand river evolution in a period of climate change (Huang et al. 2018; Langat et al. 2019; Pekel et al. 2016; Vörösmarty et al. 2003). Although river-recognition algorithms applied to satellite imagery have been indispensable tools for studying river networks, accurate delineation of rivers remains challenging due to water turbidity, the presence of vegetation, and the complexity of the landscape (Yang et al. 2015).

Open-source satellite images, such as images acquired by the Landsat series and Sentinel-2A/B, provide excellent datasets for river mapping (Pekel et al. 2014; Zhou et al. 2017). Both the retrieval frequency and spatial resolution meet the demand of observation spanning multiple scales. The delineation of small streams with a dynamic morphology rather than wide, stable rivers is more important for studies and applications related to climate change (Kuenzer et al. 2019; Pletterbauer et al. 2018). Sentinel-2A/B MSI images, with a relatively short revisit cycle (~5 days at the equator), higher resolution (up to 10 m), and high signal-to-noise ratio can facilitate the detailed delineation of global river networks (Du et al. 2016; Kaplan and Avdan 2017).

Several algorithms have been designed to extract river networks. They can be divided into four categories: (1) *Threshold segmentation based on water index (WI) images*. WI, such as the Normalized Difference Water Index (NDWI), or the Modification of Normalized Difference Water Index (MNDWI) (Acharya et al. 2018; Jiang et al. 2014; McFeeters 1996; Xu 2007). These methods rely on waterbody extraction using water-sensitive wavelengths (red, green, and NIR bands). Nones (2020) mapped the Vistula River's deposition and erosion using the MNDWI and Landsat images. Despite its simplicity and efficiency when applied to large rivers, these methods yield poor results in complex networks dissecting heterogeneous vegetated zones. (2) *Spectrum samples analysis classification*. Supervised and unsupervised water classification are two classical methods for the delineation of water bodies. Klemenjak et al. (2012) extracted river networks combining the Support Vector

Machine (SVM) and the Maximum Likelihood classification (ML) algorithms. Jia et al. (2018) proposed a spectrum matching method to distinguish water from non-water in Landsat-8 OLI images. Chen et al. (2020a) used inequality constraints on hyperspectral data to identify urban water. These methods greatly depend upon expert experience or reference samples and may not work well in small rivers with low contrast or in ungauged watersheds. (3) Morphological feature extraction. Geometric indicators (e.g., curvature, edges measured at multiple scales) are a perfect tool to delineate rivers. Passalacqua et al. (2010, 2012) extracted channel networks through curvature analysis of geomorphic features, nonlinear multi-scale filtering, and geodesic optimization. Yang et al. (2014) and Liu et al. (2015) applied the multi-scale Gaussian-Matched Filtering method and an adaptive river extraction threshold. Isikdogan et al. (2017) developed a river analysis and mapping engine using curvilinear structure to obtain water bodies and channel width. Rishikeshan and Ramesh (2018) adopted mathematical morphological techniques based on water body edges. Morphological features are useful for river extraction, but multiple dimensions and variable curvatures were seldom combined. (4) Neural network and machine learning. Machine learning is a data-driven approach, which is popular for object identification. Jiang et al. (2018) used a multilayer perceptron neural network to identify surface water in Landsat-8 OLI images. Chen et al. (2020b) introduced extraction of spatiotemporal variations of water surfaces based on the Multitemporal remote sensing imagery and delineate (EMID) method to obtain river networks. The core methodology of EMID is a random forest model based on water-occurrence frequency. River pixels omission and discontinuity are usually present in the final results due to complex backgrounds and dendritic river patterns. Admittedly, the aforementioned river extraction algorithms perform well in specific landscapes, especially for large rivers where the presence of water is evident. The performance of these algorithms may be lower in river networks spanning multiple scales, with various curvature, and dissecting a heterogeneous background. Previous studies have introduced some geometric indicator analyses, such as Gaussian match filtering, mathematical morphological analysis, curvature analysis, to enhance river network detection performance. However, few of them take into consideration the above challenges in a holistic way.

85

86

87

88

89

90

91

92

93

94

95

96

97

98

99

100

101

102

103

104

105

106

107

108

109

110

111

To address the challenges in detecting river networks (i.e., heterogeneous backgrounds, multi-scale morphology, and varying curvatures), we propose an adaptive multi-scale region growth method (AMRMG). Specifically, we use a water index (NDWI) to enhance river bodies information; a bias-corrected fuzzy C-means

(BCFCM) method mitigates the heterogeneity of the background; a scale-enhancement technique based on the Hessian Matrix to make full use of scale and direction information, and a region growth criterion to smoothly handle various river dimensions. Seldom river extraction algorithms have taken both river enhancement and pixel direction into account; the AMRGM successfully combined both strategies. As shown in applications over heterogeneous backgrounds with complex river networks, the AMRGM has proven its robustness, especially for the detection of small river branches with low contrast in the images.

#### 2. Study area and material

#### 2.1 Test sites

The accuracy of river detection methods is limited by the variability of river morphology and the heterogeneity of adjacent landscapes. Here, eight sites with complex river networks are chosen to assess the performance of the proposed AMRGM (Fig. 1a, Table 1). River morphology and geographical location were two important considerations in site selection. Testing sites include linear rivers interspersed among ponds, tidal channels in coastal zones, anastomosing branches dissecting vegetated areas, and braided rivers flowing on bare lands. Given that landscape traits are spatially varying, sites are chosen from a coastal zone, an inland area, a rainforest, a delta, a desert, and a plateau. Many classifications have been proposed for river morphology (Nardini et al. 2020; Rinaldi et al. 2016; Rosgen 1994); here, we use the classification system proposed by Rinaldi et al. (2016):

Table 1. Test site characteristic and dataset from Sentinel 2A/2B MSI. Climate type refers to Koeppen Climate System.

Number	Test sites	Background	Climate	Tile	Date	River type
1	Canada	Ponds, shallow	Subarctic	08WMA, 08WMB,08WNA	07/23/2018	Thread
2	America	Salt marsh	Humid subtropical	17RKN	12/23/2018	Wandering
3	Brazil	Rainforest	Tropical monsoon	22MEE	08/17/2019	Branching
4	England	Salt marsh	Oceanic	30UYD	05/07/2018	Thread
5	Guinea-Bissua	Bare land	Tropical wet and dry	28PDT	02/24/2019	Thread, Creek
6	Bangladesh	Mangrove	Tropical wet	48PYS	01/14/2016	Wandering
					03/24/2016	
7	Vietnam	Mangrove forest	Tropical wet and dry	45QYE	02/01/2019	Wandering
8	China	Bare land	Cold desert	46SBA	07/24/2018	Braided

- 131 (1) Mackenzie River in the Northwest Territories, Canada (Fig. 1b). The Mackenzie River basin has numerous
- anastomosing channels, wetlands, and floodplain lakes fed by snowmelt (Abdul Aziz and Burn 2006). Its
- width ranges from a minimum of 20 m to a maximum of 2.6 km.
- 134 (2) The Suwannee River in Florida, USA (Fig. 1c), is a black-water river debouching in a salt marsh coast with
- river width ranging from 10 m to 230 m (Wright et al. 2005).
- 136 (3) Amazon River in the State of Pará, Brazil (Fig. 1d), with many anastomosing branches covered with dense
- tropical rainforest. Areas near the river are frequently flooded because of the rainforest climate (Hou et al.
- 2018). The width of the Amazon river network ranges from 10 m to 1.5 km at the widest point.
- 139 (4) River Welland in the eastern part of England (Fig. 1e). The Fenland Basin is crossed by several major gravel-
- bed rivers that accrete due to tidal lag deposits (Briant et al. 2018; Plater et al. 1994). The width of the River
- Welland ranges from 10 m to 190 m.
- 142 (5) Geba River in Quinara Region, Guinea-Bissau (Fig. 1f), is characterized by a semi-arid climate with cold-
- rainy and hot-dry seasons. The river network is complex with both large and narrow streams (Zúquete et al.
- 144 2017). The width of the Geba River is 5 km at its widest channel.
- 145 (6) Ganges Delta in Bangladesh (Fig. 1g) has a complex network of distributary channels, forming a labyrinth
- of creeks, swamps, lakes, and flood plains. Its maximum width exceeds 6 km (Fagherazzi 2008; Harvey et
- al. 2005; Umitsu 1993).
- 148 (7) Can Gio Mangrove forest southeast of Ho Chi Minh City, Vietnam (Fig. 1h). The Can Gio reserve is affected
- by the tropical monsoon climate, has a high density of river channels intertwined with a thick mangrove
- forest (Thanh-Nho et al. 2019). The channel width ranges from 10 m to  $\sim 1 \text{ km}$ .
- 151 (8) Zagya Zangbo River in Tibet, China (Fig. 1i). The Zagya Zangbo River discharges into the Siling Co lake,
- and it is a classic braided river formed by glacier meltwater and precipitation (Mi et al. 2019). The width of
- the Zagya Zangbo River is close to 1.3 km in its widest channel.
- Typically, (i) sites in silty areas or along temperate salt marshes are characterized by single-thread, sinuous,
- and meandering channels. These channels can be easily misclassified due to abundant suspended sediment and
- the presence of hydrophyte vegetation; (ii) sites in tropical rainforests or subject to a subtropical monsoon climate
- have a typical branching network with meanders. The spectral difference between the river and its background

makes mapping relatively easy; and (*iii*) the Tibet plateau site has a classic braided river network, which significantly increases the heterogeneity in the image, making channel delineation difficult. A detailed description of the sites is presented in Table 1. The fluvial features of the River Welland, UK, are the most difficult to delineate because of the complicated background and intricate drainage system (Fig. 1). As a result, we choose this system to discuss our AMRGM's performance (Fig. 1e).

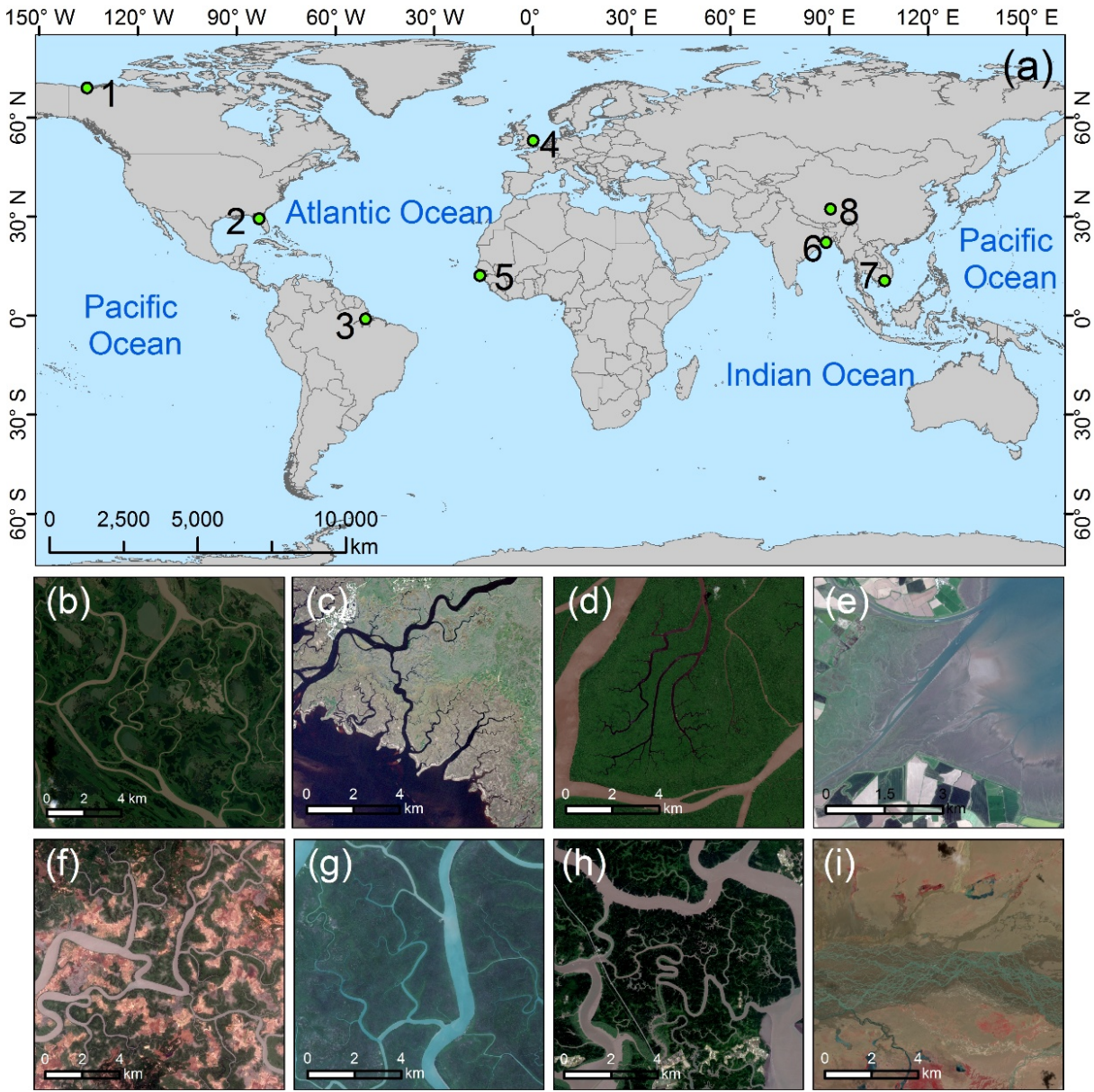


Fig. 1. (a) Map of the study sites; (b) Mackenzie River in the Northwest Territories, Canada; (c) Suwannee River in Florida, USA; (d) Amazon River in the State of Pará, Brazil; (e) River Welland in England; (f) Geba River in the Quinara Region, Guinea-Bissau; (g) Ganges Delta in Bangladesh; (h) Can Gio Mangrove forest in Vietnam; (i) Zagya Zangbo River in Tibet, China.

#### 2.2 Satellite dataset

The ESA Sentinel-2 satellites provide important datasets for terrestrial mapping. The Sentinel-2A/B MSI images come in three resolutions: four bands at 10 m, six bands at 20 m, and three bands at 60 m from visible to near-infrared wavelengths (<a href="https://sentinel.esa.int/web/sentinel/missions/sentinel-2">https://sentinel.esa.int/web/sentinel/missions/sentinel-2</a>). Instrument's radiometric differences between Sentinel-2A/B and Landsat 8 OLI is < 1%, and the former is characterized by a higher absolute geodetic accuracy (Drusch et al. 2012; Griffiths et al. 2019). Clear sky is necessary to acquire an optical image of the Earth's surface since clouds or atmospheric haze can obscure the observed targets and decrease the algorithm accuracy. Only the 10 m spatial resolution bands (Band 2: 490 nm, Band 3: 560 nm, Band 4: 665 nm, and Band 8: 842 nm) are used to map river networks. The Top Of Atmosphere (TOA) reflectance product of Sentinel-2 L1-C is used after radiometric calibration and orthographical correction; the atmospheric correction is implemented in ENVI 5.5.

## 3. Adaptive Multi-Scale Region Growth Method (AMRGM)

Heterogeneous river backgrounds, multi-scale morphologies, and the variable curvature of the channels significantly increase the difficulty in delineating river networks. To address these challenges, we adopt the following targeted optimization which enhances the extraction robustness (Fig. 2). The optimization includes four steps: (i) Water index (e.g. NDWI) is a simple but effective indicator for river extraction (Gao 1996; McFeeters 1996; Watson et al. 2018). Note that a water index can only detect the wet channels (i.e. channels filled with water) using the water spectral properties. However, the wet channels are only one of the morphological units of a river. The active channels include areas that might be dry at the time of image acquisition, as well as sediment bars and vegetated and non-vegetated islands (Hooshyar et al. 2015; Spada et al. 2018). (ii) Previous applications have proven that the Bias-corrected Fuzzy C-means (BCFCM) can effectively mitigate the ambiguity of heterogeneous backgrounds (Yang et al. 2015). Therefore, the BCFCM is applied to the NDWI image to highlight river bodies. Initial seed points are directly generated from the BFCM image. (iii) Multi-scale linear features and extension direction can be well described by the second-order derivative in the Hessian matrix (Frangi et al., 1998; Manniesing et al., 2006; Kerkeni et al., 2016). Hence, a scale-enhancement based on the Hessian Matrix is adopted to make full use of scale and direction information. (iv) Finally, a region growth criterion based on the multi-scale and direction information derived from step (iii) is adopted to segment

rivers with various dimensions. Once scale boundary conditions are given, region growth is implemented. Here, we propose a "fast-growing and fine-screening" strategy to accelerate the river network extraction and exclude outliers among river candidate pixels. This strategy makes sure that seed points grow smoothly.

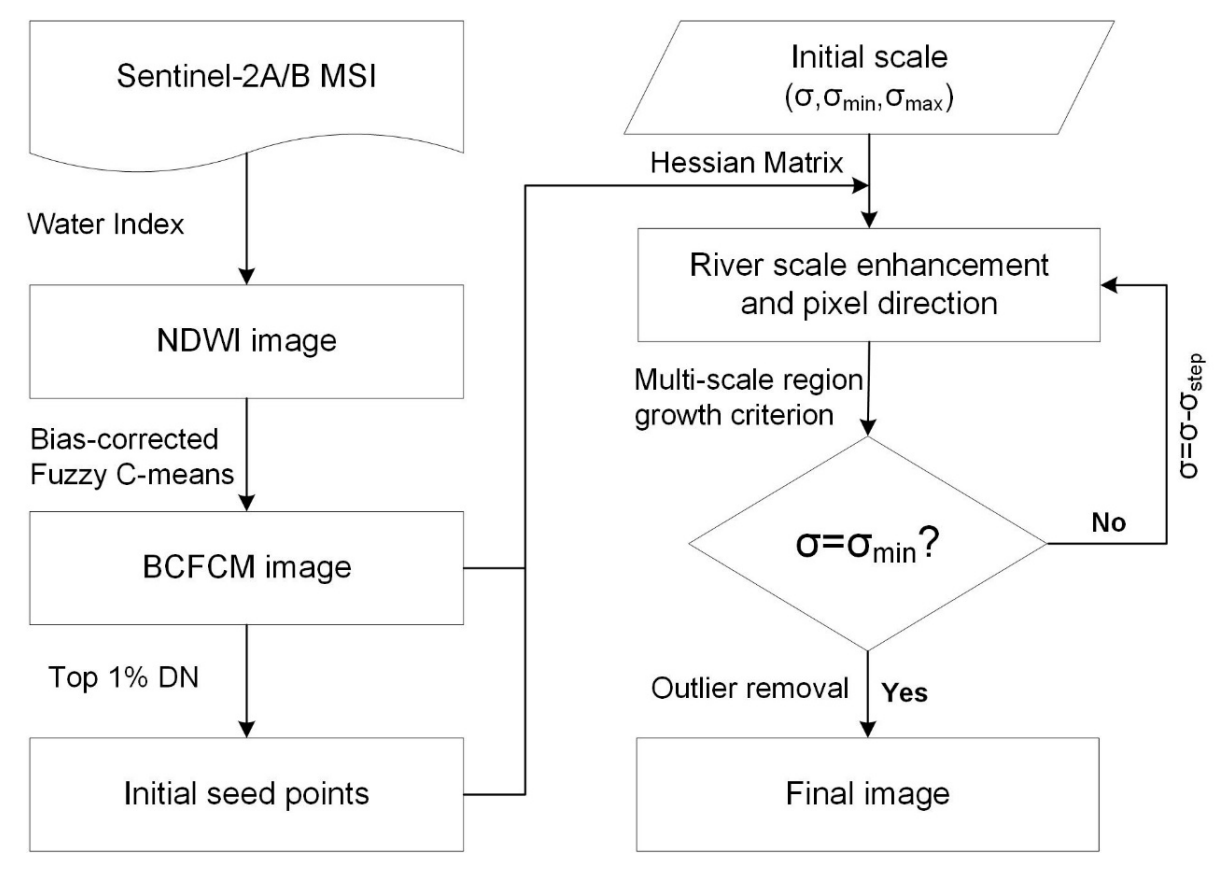


**Fig. 2.** Procedure of the AMRGM, from river enhancement, seed points generation, multi-scale region growth, and outlier removal.

#### 3.1 Fluvial features enhancement and background homogenization

Band 3 (Green Band) and Band 8 (NIR band) are used to obtain the NDWI index (Eq. 1).

$$NDWI = \frac{Band3 - Band8}{Band3 + Band8} \tag{1}$$

To enhance the difference between water bodies and surrounding landforms, we use background homogenization that unifies the representation of features through a biased field correction. A basic formula (Eq. 2) is given as follows for image (I) and the spatial heterogeneous trait ( $\beta$ ):

$$I_k = x_k + \beta_k \tag{2}$$

where  $x_k$  represents the pixel's ideal feature. Gradually varying environments can be generally regarded as a piecewise-constant model, and site-specific local variability is represented as the region-based cluster center by constant parameters  $\{v_i\}_{i=1}^c$ . The classic intensity-dependent fuzzy C-means (FCM) algorithm designs a continuum of the degree of membership ranging from 0 to 1 for each pixel (Eq. 3):

213 
$$J = \sum_{i=1}^{c} \sum_{k=1}^{N} u_{ik}^{p} \|x_{k} - v_{i}\|^{2}$$
 (3)

where  $\{u\}_{ik}^p$  is the membership of pixel  $x_k$  belonging to the type  $v_i$ . To regularize the FCM algorithm, a term compensating the adjacent coherence is incorporated into the global objective function (Eq. 4):

$$J = \sum_{i=1}^{c} \sum_{k=1}^{N} u_{ik}^{p} \|x_{k} - v_{i}\|^{2} + \frac{\alpha}{N_{R}} \sum_{i=1}^{c} \sum_{k=1}^{N} u_{ik}^{p} \left( \sum_{x_{r} \in N_{w}} \|x_{r} - v_{i}\|^{2} \right)$$
(4)

where  $N_w$  represents all the pixels in the neighborhood of  $x_k$ , and  $N_R$  is the corresponding total number of pixels,  $\alpha$  controls the degree of neighborhood effect. The whole image domain achieves optimal partition by minimizing the sum of weighted inter-class derivations (Ahmed et al. 2002). Adding Eq. 2 to Eq. 4, the bias-corrected fuzzy C-means (BCFCM) object function is computed as Eq. 5:

221 
$$\arg \min J = \sum_{i=1}^{c} \sum_{k=1}^{N} u_{ik}^{p} \|I_{k} - \beta_{k} - v_{i}\|^{2} + \frac{\alpha}{N_{R}} \sum_{i=1}^{c} \sum_{k=1}^{N} u_{ik}^{p} \left( \sum_{x_{r} \in N_{w}} \|I_{r} - \beta_{r} - v_{i}\|^{2} \right)$$
 (5)

We then iteratively calculate the membership  $u_{ik}$  in each pixel and simultaneously estimate the heterogeneous property  $\beta_i$ . The desired homogenized result is derived by subtracting the image I to  $\beta$ .

After applying the NDWI algorithm to the Sentinel-2A MSI image, the brightness difference between the target river and adjacent background becomes apparent compared to the original RGB image (Fig. 3a). The trace of the river channels is visible, but small-scale creeks or tributaries are nearly imperceptible because of the low contrast with respect to the background. Multi-modal heterogeneity appears in the histogram of the NDWI image, with the left (-0.6) and right peaks (0.4) representing the dark background and the bright river network (Fig. 3b). Brightness pixels between (-0.2) and (0.2) are difficult to be attributed to either river or landscape. Small-scale rivers will be more apparent since the fluvial background is significantly smoothed using the BCFCM procedure. As a result, two independent grey peaks at (-0.4) and (0.3) occur in the BCFCM image histogram (Fig. 3c-d).

Although the background's complexity is reduced after the background homogenization, simple threshold segments cannot identify small scale rivers (Fig. 3c).

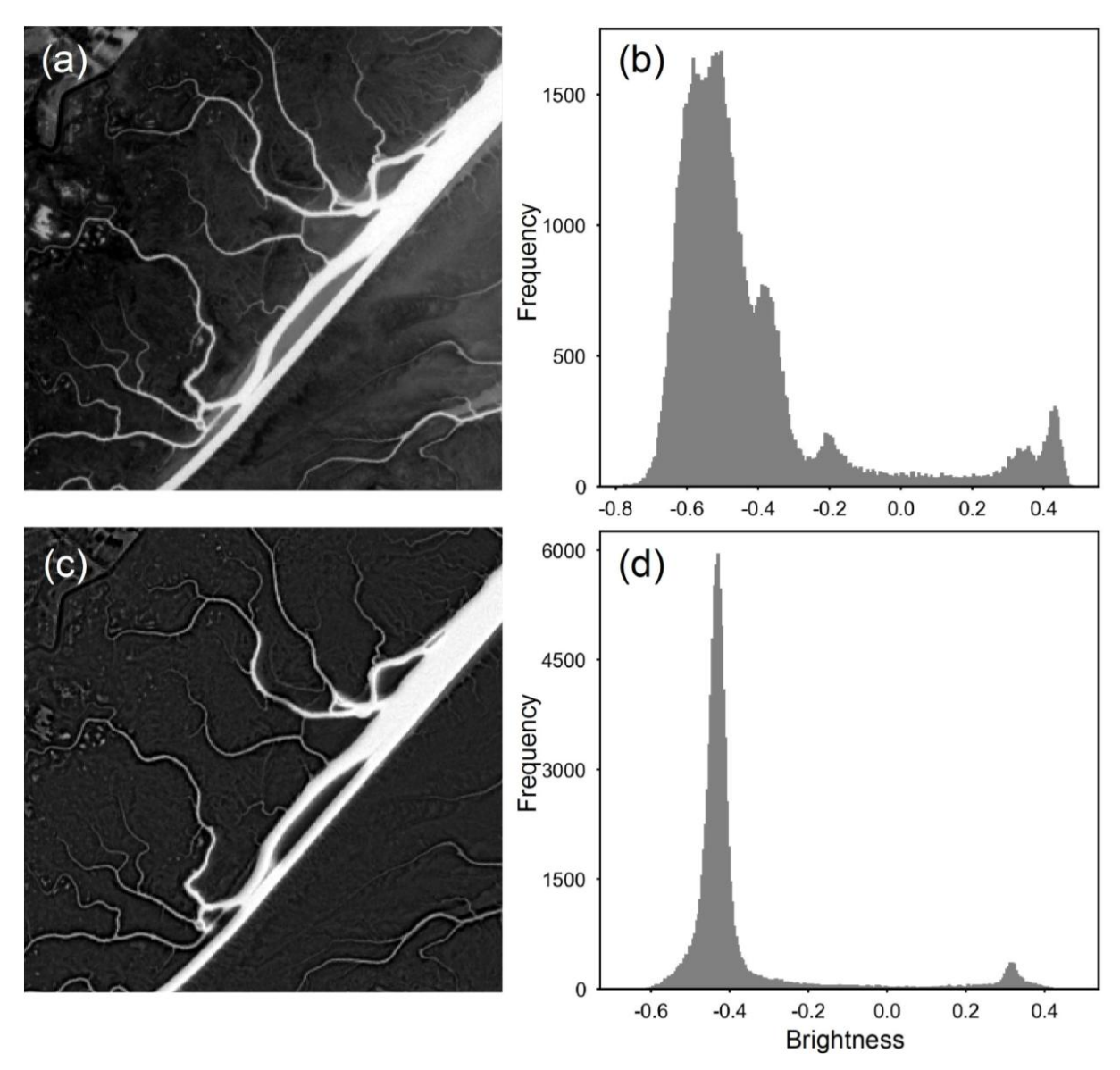


**Fig. 3.** Background homogenization: (a) NDWI image. (b) Histogram of the NDWI image. (c) BCFCM image. (d) Histogram of the BCFCM image.

## 3.2. Multi-scale river enhancement and direction analysis

#### 3.2.1 Hessian Matrix

The Hessian Matrix can be used to improve the multi-scale detection of river networks with a large range of widths. The method is based on the convolution of the original image  $I_0(x, y)$  with the 2D Gaussian kernel  $G_{\sigma}(x, y)$  (Eq. 6) (Malladi and Sethian 1995; Zhu et al. 2017).

$$I_{\sigma}(\mathbf{p}) = I_{\sigma}(\mathbf{x}, \mathbf{y}) = I_{0}(\mathbf{x}, \mathbf{y}) \otimes G_{\sigma}(\mathbf{x}, \mathbf{y})$$
(6)

243 where  $\sigma$  is the scale-kernel,  $I_{\sigma}$  is the intensity image corresponding to that scale kernel, and p represents the pixel location (x, y),  $\otimes$  indicates the convolution operator.  $G_{\sigma}(x, y)$  is calculated as Eq. 7:

245 
$$G_{\sigma}(x,y) = \frac{1}{2\pi\sigma^2} e^{-\frac{x^2 + y^2}{2\sigma^2}}$$
 (7)

where  $\sigma \in \{\sigma_{min}, ... \sigma_{max}\}$ ,  $\sigma_{min}$ ,  $\sigma_{max}$  is the minimum and maximum scale kernel, and  $\sigma$  is the core factor. Within the scale-space, differentiation is defined as a convolution with derivatives of the Gaussian function (Eq. 8).

$$\left(\frac{\partial^{n_1+n_2}I(x,y)}{\partial x^{n_1}\partial y^{n_2}}\right)_{\sigma} = I \otimes \frac{\partial^{n_1+n_2}G_{\sigma}}{\partial x^{n_1}\partial y^{n_2}} \tag{8}$$

where *n* is the order of the derivatives. Each pixel calculated with the Hessian Matrix using second-order derivatives is sensitive to the local curvature variation of intensity (Eq. 9) (Frangi et al. 1998).

251 
$$H_{\sigma}(\mathbf{p}) = \begin{pmatrix} \frac{\partial^{2} I_{\sigma}(x, y)}{\partial x^{2}} & \frac{\partial^{2} I_{\sigma}(x, y)}{\partial y \partial x} \\ \frac{\partial^{2} I_{\sigma}(x, y)}{\partial x \partial y} & \frac{\partial^{2} I_{\sigma}(x, y)}{\partial y^{2}} \end{pmatrix}$$
(9)

Hessian eigenvalues  $\lambda_I$ ,  $\lambda_2$  along with the two associated eigenvectors ( $e_I$  and  $e_2$ ), are obtained from the symmetric matrix  $H_0(p)$ . Two categories appear in the grey image, either bright linear features with a dark background or dark linear features with a bright background. Nevertheless, eigenvalue  $\lambda_I$  (i.e., minimum absolute value) is nearly zero for both types, while  $\lambda_2$  (i.e., maximum absolute value) can distinguish dark features (positive response) from bright features (negative response). A pixel with  $\lambda_I \approx 0$  and  $\lambda_2 < 0$  belongs to a bright river pixel bounded by a dark background (Kerkeni et al. 2016). Otherwise, pixels belong to dark pixels bounded by a bright background.

## 3.2.2 Feature enhancement using the multi-scale local differential structure

The Hessian eigenvalues can geometrically interpret the curvatures of linear features. A bright linear river is represented as the following (Eq. 10–12) (Manniesing et al. 2006):

$$L_{\sigma} = \begin{cases} e^{-\frac{R_b^2}{2\beta^2}} (1 - e^{-\frac{S^2}{2\gamma^2}}) & \text{if } \lambda_2 < 0 \\ 0 & \text{otherwise} \end{cases}$$
 (10)

263 and

$$R_b = \frac{|\lambda_1|}{|\lambda_2|} \tag{11}$$

$$S = ||H||_{F} = \sqrt{\lambda_{1}^{2} + \lambda_{2}^{2}}$$
 (12)

where  $\beta$ ,  $\gamma$  are weighting factors for controlling the inter-influence of  $R_b$  and S. Smoothed linear features from

- $e^{-\frac{R_b^2}{2\beta^2}}$  is multiplied by  $1 e^{-\frac{S^2}{2\gamma^2}}$  to achieve the optimal filter response in both criteria (Eq. 10).
- Following the scale-space theory (scale invariance and space invariance), each scale-enhancement is normalized by Eq. 8. The maximum responses across the probed scale-space are deemed as the optimal scalematched.  $L_{\text{max}}$  (Eq. 13) is the maximum river response when the feature reaches its optimal factor scale.

$$L_{\max} = \max_{\sigma_{\min} \le \sigma \le \sigma_{\max}} L_{\sigma}$$
 (13)

- Discrepancies between the river and adjacent background are smoothed using the BCFCM, and the local multi-scale rivers are enhanced by the multi-scale local differential geometry (Fig. 4). River response (L) gradually increases with the scale factor ( $\sigma$ ), and  $\sigma = 7$  is the maximum scale for the River Welland, UK, as all river branches are enhanced at this scale (Fig. 4a–d). Adaptive multi-scale river enhancement response (L) is depicted by color features in a multi-scale image.
- Three river-network cross sections on the processed images help to illustrate river-scale enhancement (Fig. 4). Lines 1, 2, and 3 represent three channels with different scales (Fig. 4a). Line 1 is a cross section of three small rivers; Line 2 is a cross section of two mid-size rivers; and Line 3 is a cross section of a single, large river with a sand bar at its center. In Line 1, scale  $\sigma = 1$  successfully outlines the small rivers and both banks of the large rivers. So this scale is sufficient to enhance small scale rivers, and river response (*L*) across the three rivers does not change when the scale increases. The small scale ( $\sigma = 1$ ) fails to enhance the middle-scale rivers because the river response (*L*) has not reached the "true" boundaries (red dotted line) in the column of Line 2. Once line 2 reaches the optimal response scale ( $\sigma = 3$ ), it no longer changes for higher values of  $\sigma$ . Small scale factors ( $\sigma = 1, 3$ ) cannot fully capture the large rivers, which needs a larger scale (Column of Line 3). With  $\sigma = 5$ , the algorithm already fills most of the river bodies, but the river in the red circle of Fig. 4d needs a larger scale-factor to avoid separation in two branches. When confronted with such a great range of scales, it is not practical to use each scale in the algorithm because it increases the computational burden. Alternatively, a coarse

water/land segmentation using the water index can be performed in advance to identify the large channels so that they can be excluded in the following calculations.

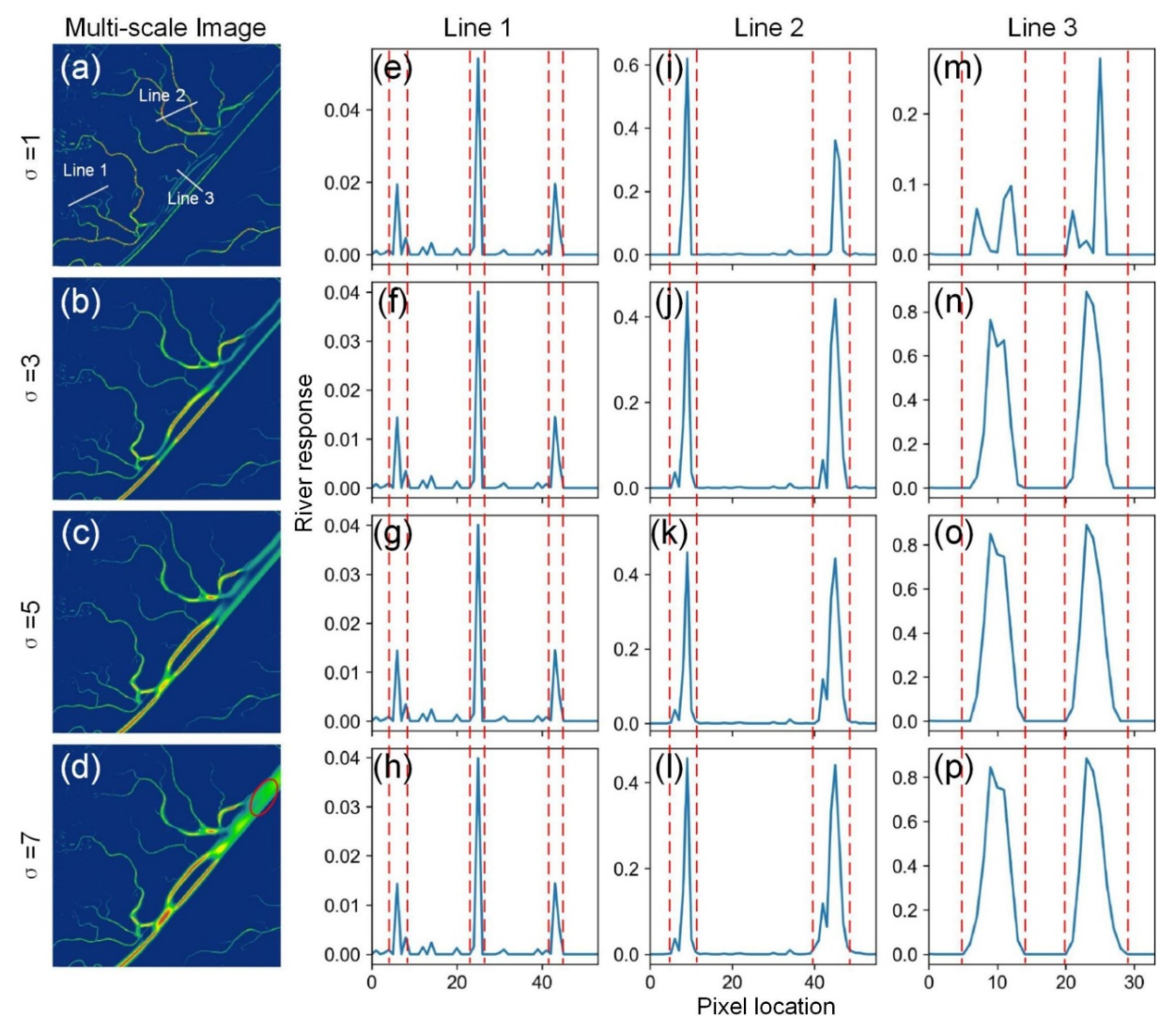


**Fig. 4.** Adaptive multi-scale local differential geometry enhances fluvial features in the River Welland, UK: (a–d) results with factor scale  $\sigma = 1, 3, 5$ , and 7, used in enhancing water bodies. Line 1, 2, and 3 cross small, mid, and large channels, respectively. Algorithm results in Line 1, 2, and 3 for each scale. The red dotted lines are river boundaries; the river response L is normalized in [0, 1].

### 3.2.3 Analysis of river pixels direction

The eigenvectors  $e_1$  and  $e_2$  of the Hessian Matrix can delineate linear structures (Eq. 9);  $e_1$  shows the direction of a potential linear structure with a low second derivative; and  $e_2$  represents the normal direction of a potential linear structure with a high second derivative (Kerkeni et al. 2016). River direction can be calculated in Eq. 14:

$$D_{\sigma}(\mathbf{p}) = \begin{cases} \mathbf{e}_{1} & \text{if } \lambda_{2} < 0 \\ 0 & \text{otherwise} \end{cases}$$
 (14)

Hessian matrix analysis not only improves the multi-scale river enhancement (*L*) but also provides pixel direction (*D*) for river water (Eq. 10, Eq. 14). Pixel directions are parallel and cover the fluvial channels with continuity and consistency (Fig. 5a–b). Pixel directions parallel the river centerline when the scale reaches its optimal value (e.g., Subset 1 Fig. 5a); otherwise, pixel directions intersect each other (Subset 2 Fig. 5c). For small-scale rivers, river scale-enhancement is weak, but pixel directions are parallel (Subset 3 Fig. 5d) and can be used for small river identification. No linear features are found in Subset 2, resulting in non-parallel pixel directions (Fig. 5c). The combination of river scale response and pixel direction dramatically improves river extraction accuracy, especially for the network of small streams with low water brightness.

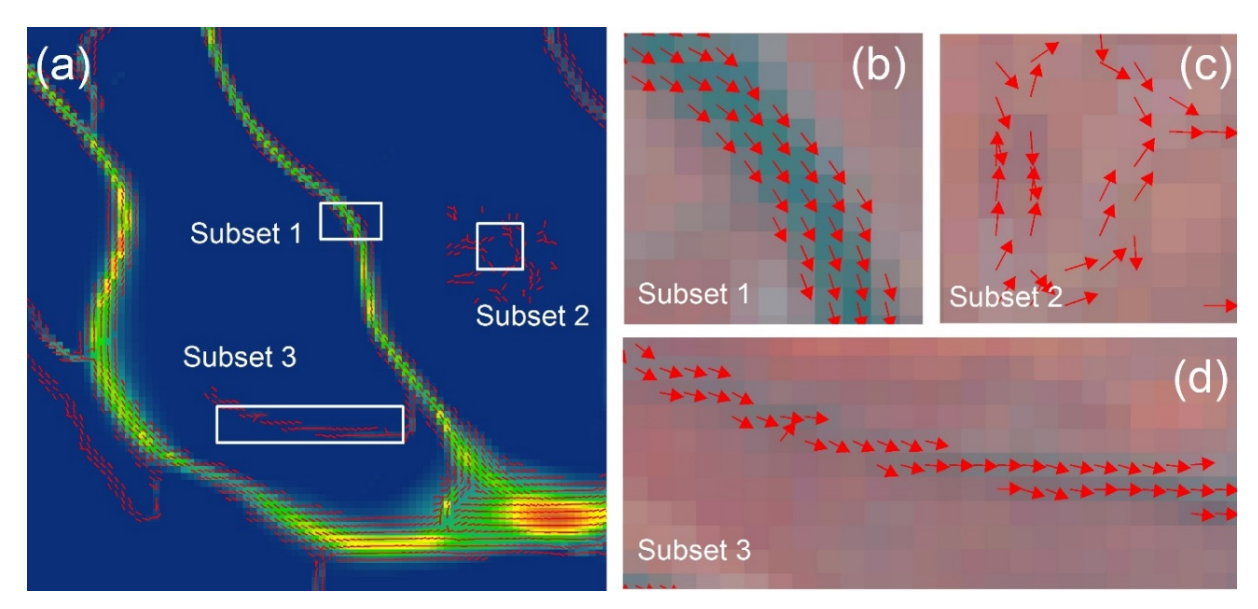


**Fig. 5.** River network direction information: (a) direction computed with the multi-scale algorithm using the local differential structure, pixel directions are consistent at the confluence between river branches and the main trunk. Note that only a fraction of pixel directions are displayed for clarity. (b), (c) and (d) represent the pixel directions in Subset 1, Subset 2, and Subset 3.

#### 3.2.4 Multi-scale regional growth algorithm

Favorable seed points are required for proper network growth, and the largest 1% of DN pixels are used here for this purpose. The seed points are mostly located in large scale rivers (Fig. 6a). A few seed points are manually added in branches that are weakly connected to the main trunk. The network starts growing from the seed points and expands from large scale to small scale branches with a fluid and fast process (Kerkeni et al.

2016; Sekiguchi et al. 2005). Network growth from the seed points is performed iteratively. After each iteration
 is executed, all the new pixels added to the network become seed points for the next round.

The use of pixel directions is indispensable to distinguish small and narrow river branches (Fig. 5c). Leveraging on this idea, a regional growth criterion is adopted using the following convergence conditions: for a seed point ("q") and a river pixel ("p"), the pixel orientation correlation index,  $\Omega_{\sigma}(p, q)$  is defined as Eq. 15.

325 
$$\Omega_{\sigma}(\mathbf{p}, \mathbf{q}) = \frac{D_{\sigma}(\mathbf{p}) \cdot D_{\sigma}(\mathbf{q})}{\|D_{\sigma}(\mathbf{p})\| \|D_{\sigma}(\mathbf{q})\|}$$
(15)

The pixel direction is parallel when  $\Omega_{\sigma}(p, q) = 1$  and perpendicular when  $\Omega_{\sigma}(p, q) = 0$ . Pixel p conforms to Eq. 327

$$p \in N_n(q) \cap L_{\sigma}(p) > \eta(1 - \Omega_{\sigma}(p, q))$$
(16)

where pixel q is set as a river pixel.  $N_n(q)$  represents the n-neighborhood pixels.  $N_4$  and  $N_8$  are used here.  $\eta$  is a threshold; a small  $\eta$  will bring overgrowth while a large  $\eta$  will underestimate neighboring pixels' extension.  $\eta$  is selected as 0.8 in the River Welland site based on the scale-enhancement results (Fig. 4). A 4-neighbor ( $N_4$ ) and 8-neighbor ( $N_8$ ) algorithm is used to obtain multiple-scale rivers (Appendix algorithm 1). The  $N_4$  aims to extract large rivers using Eq. 16, while the  $N_8$  delineates small rivers following the  $N_4$  results.

The detailed process of the multi-scale region growth is described in Appendix algorithm 1. River scale-enhancement (*L*) and pixel direction (*D*) are computed in the BCFCM image (*I*). A processing queue (*S*) is implemented to store the seed points (*B*); the seed points are deleted when the growth terminates after each iteration. The main river has a high response, whereas the small-scale rivers are easily overlooked when the pixel response is less than  $\eta(1 - \Omega_{\sigma}(p, q))$ . To address this problem, an additional growth condition  $\Omega_{\sigma}(p, q) \le \sqrt{3}/2$  (pixel direction within 30°) is used to delineate the small and narrow streams ( $\sigma = 1, 3$ ). Two piecewise growth processes are performed in rivers with different dimensions. The first process is used to delineate the brightness of wide rivers, while the second one is sensitive to small-scale branches (Appendix algorithm 1). The two processes significantly improve computational efficiency.

The step-wise progression of the multi-scale rivers growth algorithm is illustrated in Fig. 6 and encompasses seed point generation, river pixel growth, and outlier removal. To help visualization, we keep the NDWI image as the background and implement the AMRGM in the BCFCM image. Initial seed points are automatically

generated in mid-size rivers, and we manually add some pixels at the top right corner (Fig. 6a). The network grows from the seed points and quickly expands in the large rivers ( $\sigma$  between 5 and 7, Fig. 6b–c). The small branches of the River Welland are characterized by low NDWI and weak linearity (Fig. 3c), so they cannot be easily captured by Eq. 16 until river growth termination. Considering pixel direction is less affected by the river's brightness, the orientations correlation index ( $\Omega$ ) is a better indicator for distinguishing the remaining small branches (Appendix algorithm 1). A large number of small branches grow when  $\sigma = 3$  (Fig. 6d), compared to  $\sigma = 5$  (Fig. 6c). A scale  $\sigma = 3$  nearly reaches the optimal result as few pixels are added from  $\sigma = 3$  to  $\sigma = 1$  (Fig. 6e). Many subtle channels draining in the main stem also form: for example, the small branches at the top right corner of the image. Excessive pixel growth inevitably occurs at both sides of the large-scale rivers following the "fast-growing and fine-screening" strategy (Fig. 6e). As the AMRGM will extract all potential river pixels, the excessive pixels need to be removed at the end of the growth (outlier removal).

A sliding window (10 × 10 pixels) is used to screen pixel belonging to large or small scale streams in the BCFCM image (Appendix algorithm 2). The most important step is splitting the extraction of pixels into small or large rivers. If the maximum value within the sliding window ( $I_{max}$ ) exceeds the threshold M (0.1), and pixel response  $I_p$  is below the threshold  $T_1$  (0.3), the pixel is removed (outlier nearby a large-scale river). If the  $I_{max}$  is less than M, the pixel pertains to a small-scale river, and then a simple threshold  $T_2$  (-0.02) is directly adopted to delete the extra pixels (Fig. 6f). Values in brackets represent the parameters used in the River Welland basin.

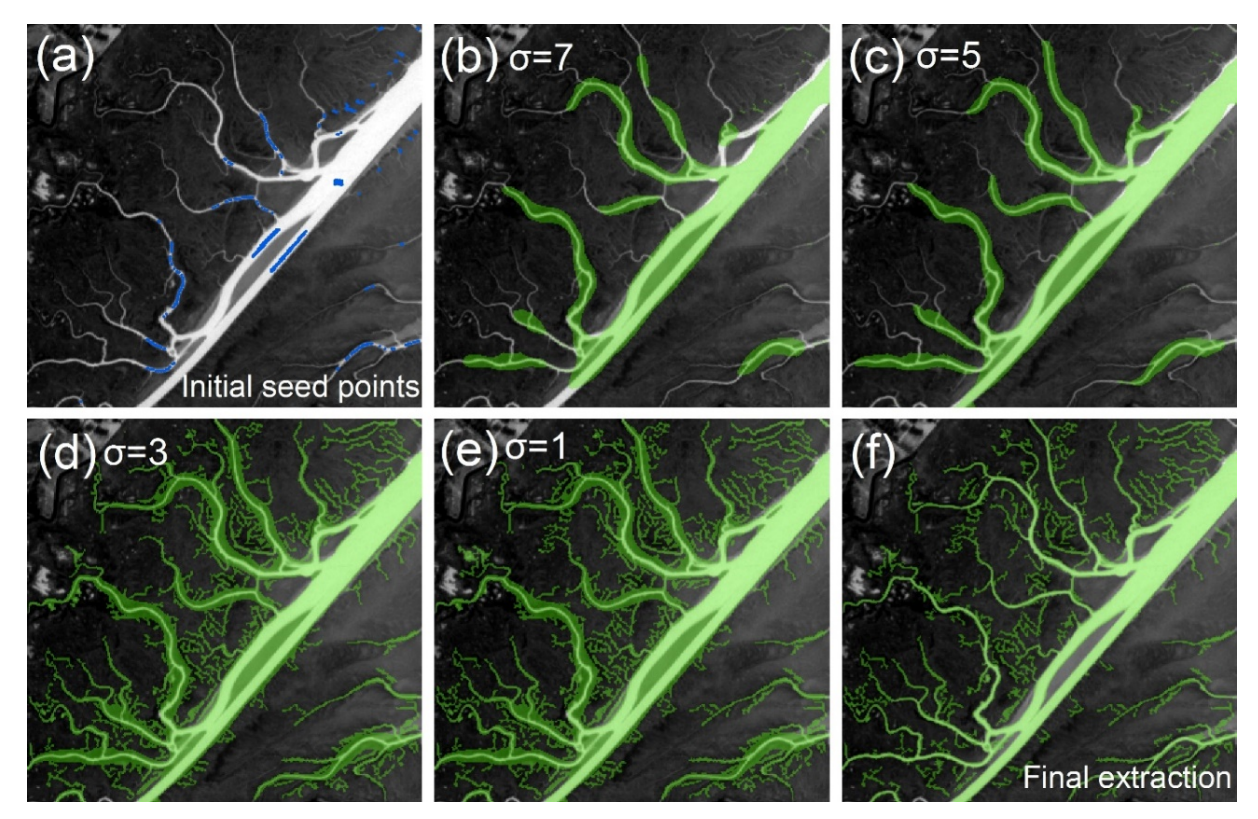


**Fig. 6.** Process of region growth in the River Welland network: (a) Initial seed points (blue pixels) automatically generated from the BCFCM image and with some few points added in small rivers. (b-e) River pixels (green pixels) expanding from large-scale channels into small-scale streams. (f) Outlier removal result.

# 4. Implementation of the AMRGM

#### 4.1 Extraction of the River Welland network

Since a comparison between the algorithm results and ground truth data is more meaningful at the same spatial scale, we select the Sentinel-2A MSI color composite image as the base map for ground truth data to evaluate the accuracy of the river extraction. Visual interpretation is widely adopted as a benchmark in various RS classification/extraction applications. We therefore manually delineate the channels in the ground truth image. All the river networks extracted with the AMRGM are "wet channels", and might change in time with water levels (Fig. 6). The misclassified and missing pixels are attributed to commission and omission errors. When the water level is low, the edge of sand bars and river banks appear as bright linear features. Commission errors are mainly distributed near these landforms because the algorithms identify them as river pixels due to the linear texture and direction properties. On the other hand, omission errors mainly occur in a small creek along the trunk because of excessive pixel removal (Appendix algorithm 2). Not all small branches are found by our algorithm

(Fig. 7a). Most river pixels are captured during the multi-scale region growth procedure in Fig. 6e, but only a few disconnected patches and non-identified channels are present in the final map after outliers removal (Fig. 7b). Several small streams are identified by the AMRGM but are not captured by the manual classification in the color composite image. The river extraction is carried out at high tide to capture active channels that might be dry at low tide. If we select an image taken at high tide, the river's background becomes blurry, decreasing the accuracy of the AMRGM (See Fig. S1 of Supplementary Materials for details).

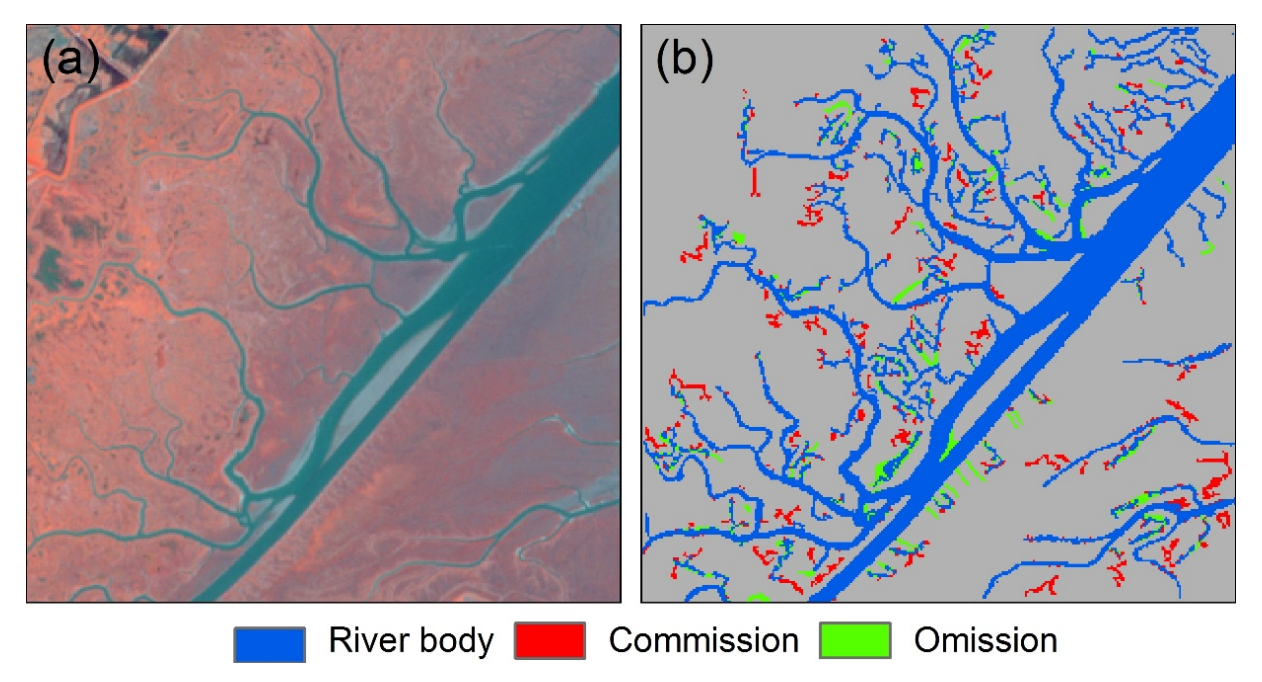


**Fig. 7.** Extraction of the network in the River Welland using the AMRGM: (a) Color composite image (R: Band 8, G: Band 3; B: Band 2); (b) Accuracy analysis obtained after comparison with the ground truth image. Red pixels represent commission errors, while green pixels are omission errors.

#### 4.2 Performance of the AMRGM in seven sites

The AMRGM is then applied to seven new sites divided into two classes based on the basin area covered by the remote sensing images. Small sites contain the Suwannee River, the Amazon River, the Can Gio Mangrove, and the Zagya Zangbo River (Fig. 8); large sites include the Mackenzie River, the Geba River, the Ganges Delta; all of them possess an area exceeding 800 km² in the remote sensing images (Fig. 9). Channel extraction is carried out using five methods (AMRGM, SVM, ML, ISODATA, KM). Of all methods tested, the AMRGM performs the best, followed by the SVM (Fig. 10); only the AMRGM and SVM extraction results are displayed in Fig. 8–9.

The middle and large-scale channels in the Suwannee River, Amazon River, and Can Gio Mangrove forest are relatively linear (Fig. 8), whereas the low-order creeks in the Suwannee River are characterized by meanders (Fig. 8a1–a2). In Subset area 1 and Subset area 2 of the Suwannee River, the AMRGM easily captures the small meandering creeks, while the SVM performs poorly (Fig. 8a3–a6). In the Amazon River (Fig. 8b1), the river network is dendritic with sharp width transitions from the main channels to the tributaries (Fig. 8b2). Here, several streams are not captured by the SVM (Subset area 1 and Subset area 2, Fig. 8b4 and b6). In contrast, the AMRGM detects streams at all dimensions (Fig. 8b3 and b5). Similar results are also obtained in the Can Gio Mangrove forest (Fig. 8c1), where the AMRGM delineates a large number of small-scale streams (Fig. 8c3 and c5) that are missed by the SVM (Fig. 8c4 and c6). The Zagya Zangbo River in Tibet has a complex river network with a high number of braided channels formed by sediment deposition and erosion; our method obtains better results for this system compared to the SVM (Fig. 8d1–d2). The river networks are more evident after the background homogenization performed by the AMRGM (Fig. 8d3 and d5 vs. Fig. 8d4 and d6). In general, the AMRGM performs well in large rivers (Fig. 10), where the water area has very distinct optical properties. However, sometimes it fails at delineating small channels with a limited water surface.

In the large study sites, the small rivers cannot be recognized in the composite color image (Fig. 9). The Mackenzie River site is characterized by linear streams with different dimensions and lakes scattered across the landscape (Fig. 9a1). The water bodies are clearly extracted with the AMRGM (Fig. 9a2) in Subset area 1 and Subset area 2 (Fig. 9a3 and a5). The SVM performs poorly in small streams and ponds because of the similar spectral characteristics compared to the surrounding areas (Fig. 9a4 and a6).

The Geba River basin includes multiple river patterns, with small creeks and linear channels. The area surrounding the channels is characterized by diverse land uses and vegetation, which complicate the river networks' extraction (Fig. 9b1). Elongated streams also characterize the Geba River, and the AMRGM successfully delineates its complex network (Fig. 9b2). In the subset regions, the AMRGM performs much better than the SVM at the tip of small tributaries (Fig. 9b3–b6). In the Ganges delta site, the spectral difference between river and background is not as apparent as for the other sites. The SVM recognizes the relatively wide rivers (Fig. 9c4 and c6), but our method achieves a better result in small distributaries (Fig. 9c2, c3, c5).

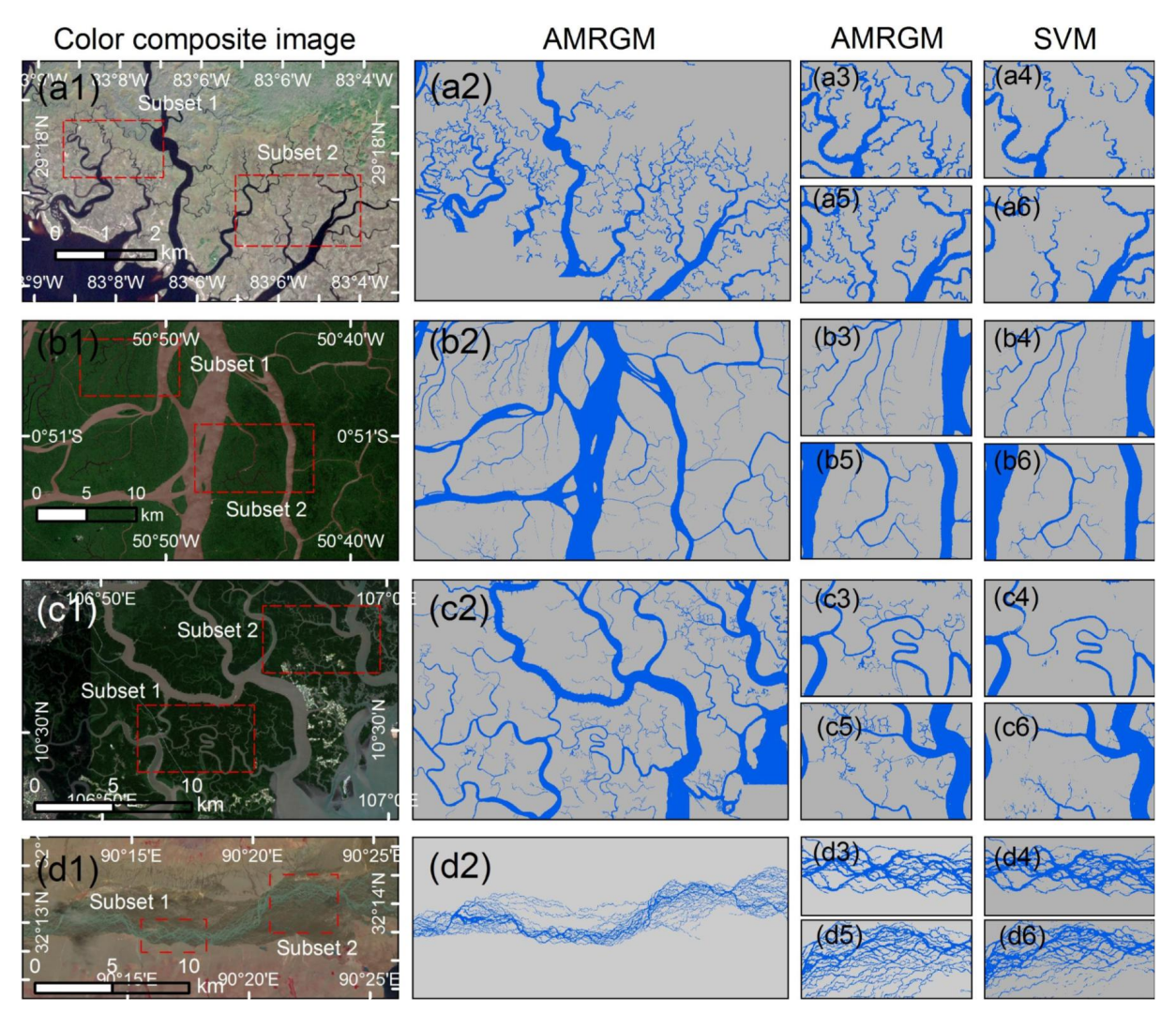


**Fig. 8.** Comparison of river networks in small basins extracted with the AMRGM and SVM from remote sensing images: (a1) color composite image of the Suwannee River; (a2, a3, a5) Suwannee River network, Subset 1, and Subset 2 river extraction using SVM; (b1) color composite image of the Amazon River; (b2, b3, b5) Amazon River network. Subset 1, and Subset 2 river extraction using AMRGM, (b4, b6) Subset 1 and Subset 2 river extraction using SVM; (c1) color composite image of the Can Gio Mangrove forest, (c2, c3, c5) Can Gio Mangrove forest networks, Subset 1, and Subset 2 river extraction using AMRGM, (c4, c6) Subset 1 and Subset 2 river extraction using SVM; (d1) color composite image of the Zagya Zangbo River, (d2, d3, d5) Zagya Zangbo network, Subset 1, and Subset 2 river extraction using AMRGM, (d4, d6) Subset 1 and Subset 2 river extraction using SVM.

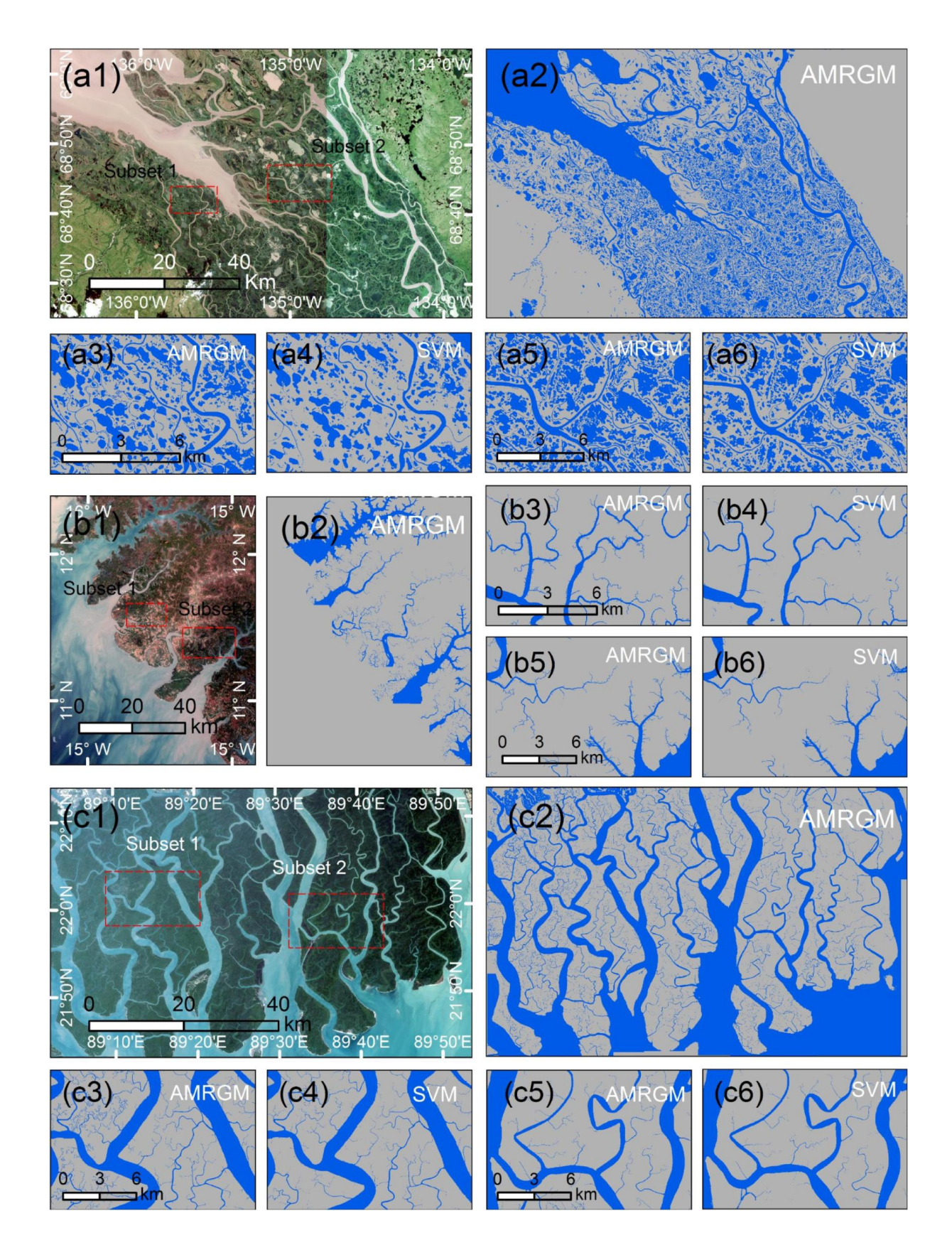


**Fig. 9.** Comparison of river networks in large basins extracted with the AMRGM and SVM from remote sensing images: (a1) color composite image of the Mackenzie River, (a2, a3, a5) Mackenzie River network, Subset 1 and Subset 2 river extraction using SVM; (b1) color composite image of the Geba River; (b2, b3, b5) Geba River network, Subset 1 and Subset 2 river extraction using AMRGM, (b4, b6) Subset 1 and Subset 2 river extraction using SVM; (c1) color composite image of the Ganges Delta, (c2, c3, c5) Ganges Delta network, Subset 1 and Subset 2 river extraction using AMRGM, (c4, c6) Subset 1 and Subset 2 river extraction using SVM.

#### 4. 3 Quantitative analysis of five extraction methods

River networks delineated by the AMRGM are compared to the results of four additional methods: (*i*) clustering method (K-means method, KM); (*ii*) unsupervised classification (maximum likelihood method, ML); (*iii*) Iterative Self-Organizing Data Analysis Technique Algorithm (ISODATA); and (*iv*) supervised classification (Support Vector Machine, SVM). Four primary classification cases are considered: true positive (TP), true negative (TN), false negative (FN), and false-positive (FP). Accordingly, the Kappa coefficient (k), the overall accuracy (OA), the Commission Error (CE), and Omission Error (OE) are calculated to assess each method (Fig. 10). The definition of each index is reported in Table 2.

**Table 2.** A quantitative index used in the assessment.

Quantitative Index	Formula	Indication
Kappa coefficient (k)	$k = (p_0 - p_c)/(1 - p_c)$	Agreement between two images
Overall accuracy (OA)	OA = (TP+TN)/N	Correctly classified pixel ratio
Commission Error (CE)	CE = FP/(FP+TP)	Pixels misclassified as the target feature class
Omission Error (OE)	OE = FN/(TP+FN)	Pixels misclassified as the non-target feature class

Note:  $p_0 = (TP+TN)/N$ ,  $p_c = ((TP+FN)\times(TP+FP)+(TN+FP)\times(TN+FN))/(N\times N)$ , (TP) true positive, (TN) true negative, (FN) false negative, and (FP) false positive.

A method for the global delineation of small scale rivers needs to be flexible and applicable to a wide range of fluvial landforms. To better assess the method's accuracy, only middle scale and small scale rivers ( $\sigma$  < 7) are chosen here in the quantitative evaluation (Pletterbauer et al. 2018). The AMRGM achieves the highest OA, KC as well as the lowest CE and OE in the eight sites. Excluding the River Welland, the AMRGM OA and KC exceed 95% and 0.91, respectively, and the mean OA and KC are about 97% and 0.92. The maximum scores are present in regions where the rivers are spectrally well separated from the background, such as in the Amazon River (OA = 99.3%, KC = 0.96) and in the Ganges Delta (OA = 98%, KC = 0.91). OA for the River Welland decreases to 93.8%, and the KC is 0.86 (Fig. 7). Among the four traditional methods, the supervised method SVM is better than the unsupervised methods ML (mean OA = 93% for SVM). The KM method is sensitive to

pixel noise, so it performs poorly in rivers with complex terrain. KM's OA also reaches 97% in the Amazon River and the Ganges delta, but it is only 67% and 61% in the Zagya Zangbo and Welland Rivers. The AMRGM performance is very high in sites with elongated rivers, particularly when streams have different dimensions (e.g., in the Suwannee River, in the Ganges delta, and the Can Gio Mangrove forest). Traditional methods fail to recognize small creeks and only extract middle and large-scale rivers (Fig. 8–9). The Suwannee River and the Zagya Zangbo River are the two most complex sites due to the high drainage density, but our method achieves better results than supervised or unsupervised methods. More extraction results with the different methods are displayed in the supplementary materials (See Fig. S2 of Supplementary Materials for details).

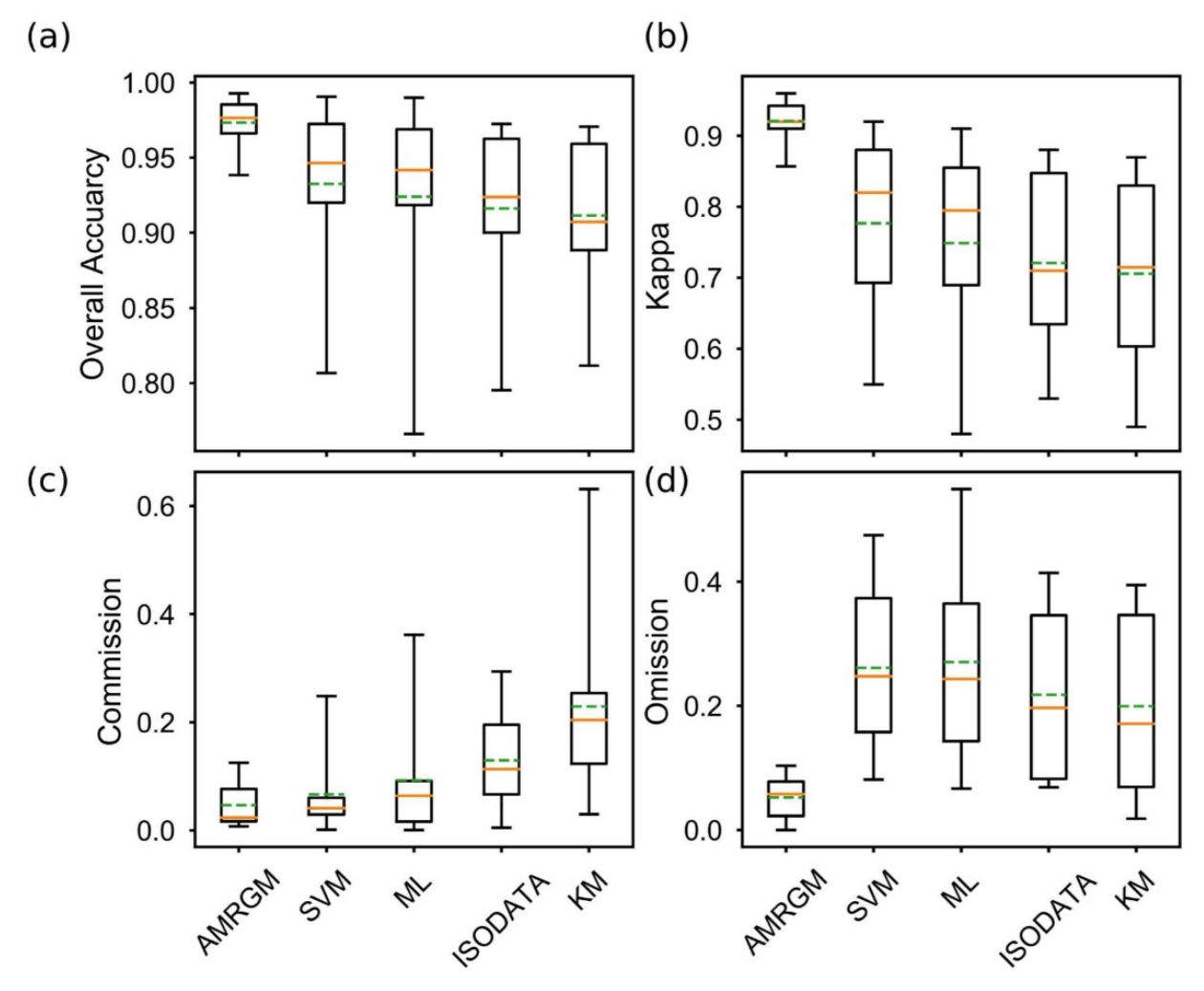


**Fig. 10.** Overall performance of AMRGM compared to four other methods: SVM, ML, ISODATA, and KM. (a)-(d) overall accuracy, Kappa coefficient, commission, and omission errors for the eight sites. The orange line represents the median, and the green dotted line is the mean value.

#### 5. Discussion

## 5.1 AMRGM thresholds selection and river pixel changes at different scales

The AMRGM requires the selection of several thresholds to carry out background enhancement, multiscale region growth, and outlier removal. It is difficult to choose identical thresholds for all eight sites. If the threshold parameters are appointed at a large scale, relevant small streams cannot to be detected. The BCFCM image is then used for network growth and outlier removal. River pixel orientation correlation  $\Omega_{\sigma}$  is the same among all sites  $(\Omega_{\sigma}(p,q) \leq \sqrt{3}/2)$ . Consequently, a fixed threshold can generate a good result for river networks with prominent water characteristics, such as the Amazon River (Brazil), and the Suwannee River (USA). In contrast, thresholds need to be fine-tuned to avoid the omission of small rivers in networks with subtle contrast with respect to the background, such as the River Welland area (UK). Through a "trial-and-error" strategy, we can select a series of appropriate thresholds using an iterative process to suppress noise and improve extraction accuracy.

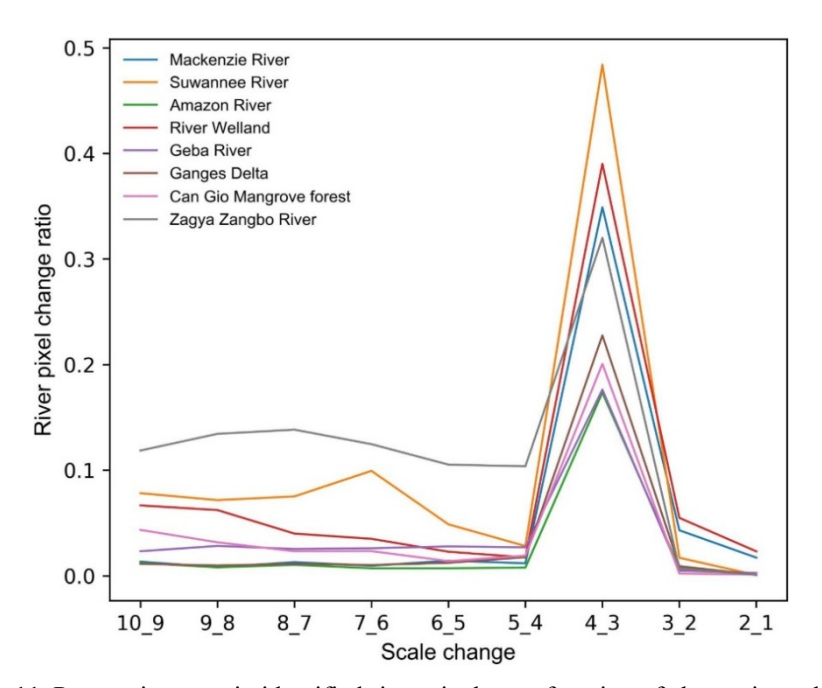


**Fig. 11.** Percent increase in identified river pixels as a function of change in scale  $\sigma$ .

In the network growth process (see Fig. 6), the number of river pixels increases faster when  $\sigma = 3$  (Fig. 11). In large-scale rivers such as the Amazon River and Ganges Delta, the percent of identified river pixels is low; in

rivers with complex geometry, the river pixel change ratio is relatively high for large  $\sigma$  scales (e.g., the Zagya Zangbo and Suwannee Rivers). Once the pixel direction is used to identify small rivers, a large pixel ratio occurs from  $\sigma = 4$  to  $\sigma = 3$ . The Change ratio peaks at  $\sigma = 3$ , and the maximum value is reached in the Suwannee River (48.4%). Excessive detection of water bodies mainly occur near the river banks, which can be flooded by changing water levels. River pixel ratio changes quickly in small rivers where only pixel directions are used.

496

497

498

499

500

501

502

503

504

505

506

507

508

509

510

511

512

513

514

515

516

495

491

492

493

494

### 5.2 River extraction uncertainty using the AMRGM on Sentinel-2A/2B images

The AMRGM is appropriate for extracting small scale rivers with low spectral features because it combines river-scale enhancement and pixels direction. However, scale effects in remote sensing imagery and dry channels may cause uncertainties in river extraction. Many secondary channels can be observed in highresolution remote sensing images (HR), but they are seldom visible in 10 m resolution images. Note that of the eight sites studied here, only two sites, i.e., the River Welland (UK) and the Suwannee River in Florida (USA), have HR images which were acquired within one month from the Sentinel-2 MSI image (Fig. 12). As expected, there are some morphological differences between the visual delineation of river networks from HR images (rivers-HR) and those visually interpreted from Sentinel-2A/B MSI images (river-MSI) (Fig. 12a1-a2, b1-b2). The AMRGM cannot discern small channels (< 5 m) because of the mixed pixels in river-MSI images. In Figure 12 we compare the network morphology extracted from rivers-HR and river-MSI images. Many small river branches can be manually extracted in the HR image of the River Welland, while the AMRMG just delineates larger streams with high brightness (~10 m) (Fig. 12a6-1-a6-2, a8-1-a8-2, a9-1-a9-2). A similar approximation also occurs in the Suwannee River because of the different resolution of the remote sensing images (Fig. 12b7-1-b7-2, b9-1-b9-2, b11-1-11-2). The difference in total channel area between rivers-HR and rivers-MSI is 7.47 km<sup>2</sup> (9.6 km<sup>2</sup> vs. 17.07 km<sup>2</sup>) for the River Welland and 8.08 km<sup>2</sup> (9.496 km<sup>2</sup> vs. 1.421 km<sup>2</sup>) for the Suwannee River. The difference in the length of the main stem is 15.6 km (45.7 km vs. 30.1 km) and 5.97 km (25.38 km vs. 19.41 km) respectively; whereas 98 km (45 km vs. 143 km) and 36 km (65 km vs. 29 km) of small tributaries cannot be distinguished from MSI images. These errors are mainly caused by different resolution of the images and by mixed pixels that prevent the identification of the streams.

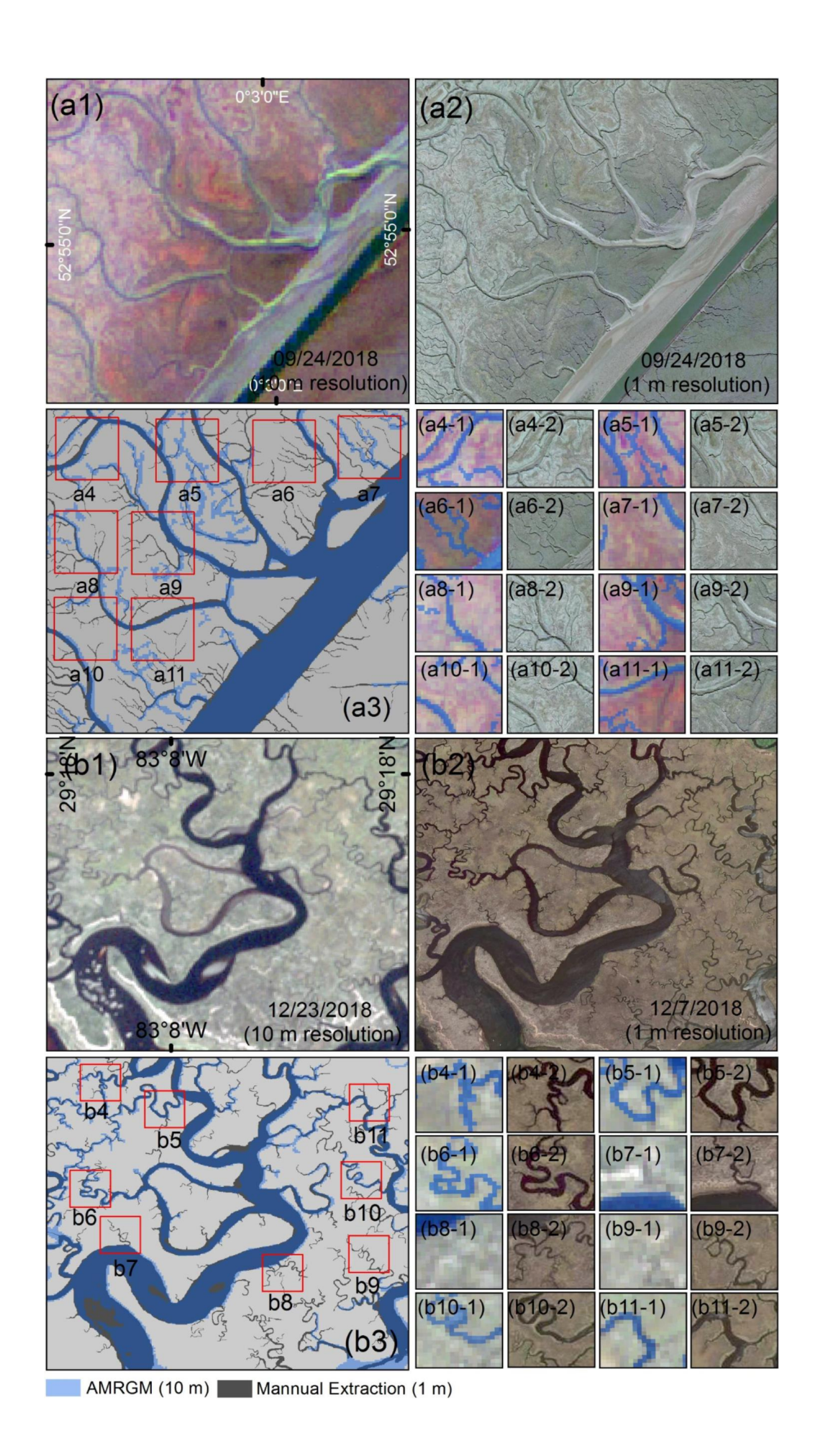


**Fig. 12.** Comparison between river delineation from Sentinel-2A MSI images using the AMRGM and HR images: (a1) AMRGM delineation from a 10 m MSI image of the River Welland (UK); (a2) Visual interpretation from a 1 m HR image (rivers-HR); (a3) AMRGM delineation overlapped to rivers-HR. The grey thin lines are rivers-HR that were not extracted by the AMRGM; (a4-1-a11-1) zoom-in of the MSI image; (a4-2-a11-2) zoom-in of the corresponding HR images with the un-extracted channels. (b1) AMRGM delineation from a 10 m MSI image of the Suwannee River (USA); (b2) Visual interpretations from a 1 m HR image (rivers-HR); (b3) AMRGM delineation overlapped to rivers-HR. (b4-1-b11-1) zoom-in of the MSI image; (b4-2-b11-2) zoom-in of the corresponding HR images with the un-extracted channels.

In the River Welland, few small streams (width < 6) can be delineated in the MSI images (2), but

many are present in the high resolution image (140) (Fig. 13a). Fewer streams with a width of 6–10 m are also extracted by the AMRGM (7 versus 39). However, there is not a significant difference in the number of streams larger than 10m (Fig. 13a). Similar results are also obtained in the Suwannee River (Fig. 13b).

Note that in the HR-images we delineate also channels that are not wet at the time of the image acquisition, since the limited spectral information does not allow to compute the NDWI index. Therefore, the number of channels in the HR-images can be higher because we detect all active channels and not only wet channels. The number of wet channels can also change in time with variations in water level. This is particularly true in tidal rivers, like the Welland and Suwanee. A comparison between images taken at different times with different water levels also produces discrepancies in the extracted channel network. However, we point out that the main difference between the HR-river and the MSI-river networks concerns the low-order streams with a width smaller than the Sentinel-2A/B resolution (Fig. 13). For channels larger than 10m the AMRGM results are excellent with respect to the HR-images. We therefore conclude that the different

resolution of the images is the main cause of error in the extracted channel networks.

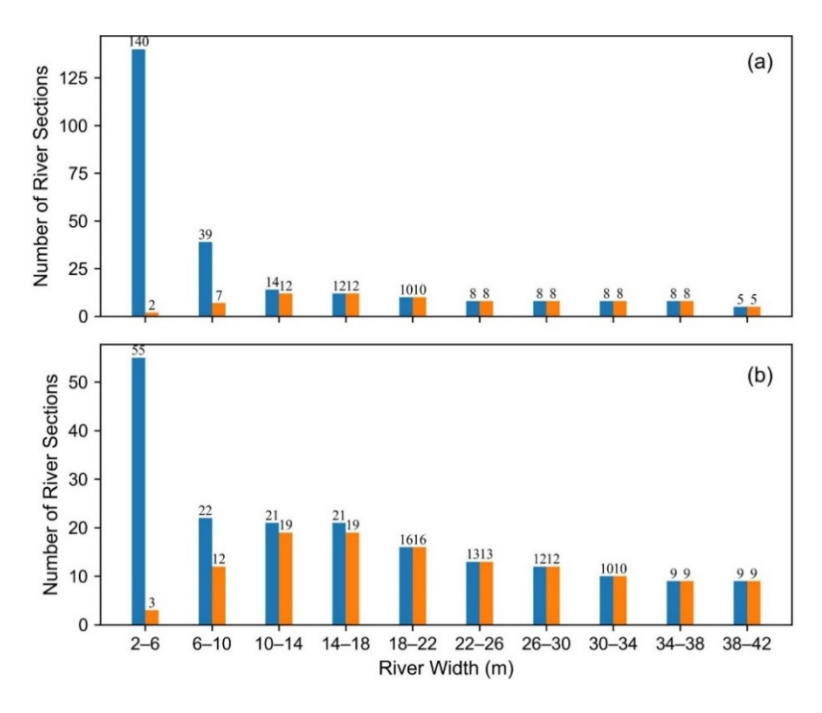


**Fig. 13.** Number of streams in the HR images (Visual interpretation) and Sentinel-2 MSI images (AMRGM). (a) River Welland. (b) Suwannee River. Some streams change width and may be counted more than once. In the HR images all active channels are delineated while the AMRGM detects only wet channels.

## 5.3 Generalization and transferability of the AMRGM

The AMRGM was initially designed to extract multi-scale linear rivers, but it can similarly extract lakes and ponds (Fig. 9a2). The boundaries of lakes and ponds are linear features, which are enhanced by the Hessian matrix. With the AMRGM seed points grow fluidly along the lake's edges. Our method can also be used to detect wadis in arid landscapes (Fig. 14). Wadis are typical in the northwestern part of the Arabian Peninsula, which has a classic sub-tropical desert climate with a mean temperature of 30 °C in summer and 13 °C in winter (Liu et al. 2016). Wadis are seasonal rivers, characterized by irregular, inconspicuous streams and weak spectral features (Fig. 14a). Wadis networks show classical anisotropy features. Because of the desert climate, vegetation is rarely present so that the NDWI can enhance the main stream of each wadi. After applying the river and background enhancement, the wadis become apparent in the original color composite image. Thousands of streams with subdue linear features and strong anisotropy are detected by the AMRGM (Fig. 14b). The results of the extraction strongly depend on the surrounding background (Fig. 14c–e). The white background of Subset 1 allows an excellent delineation of the wadis (Fig. 14c). In Subset 2 and Subset 3, the wadis dissect hillsides,

where tributary channels have irregular morphological features.

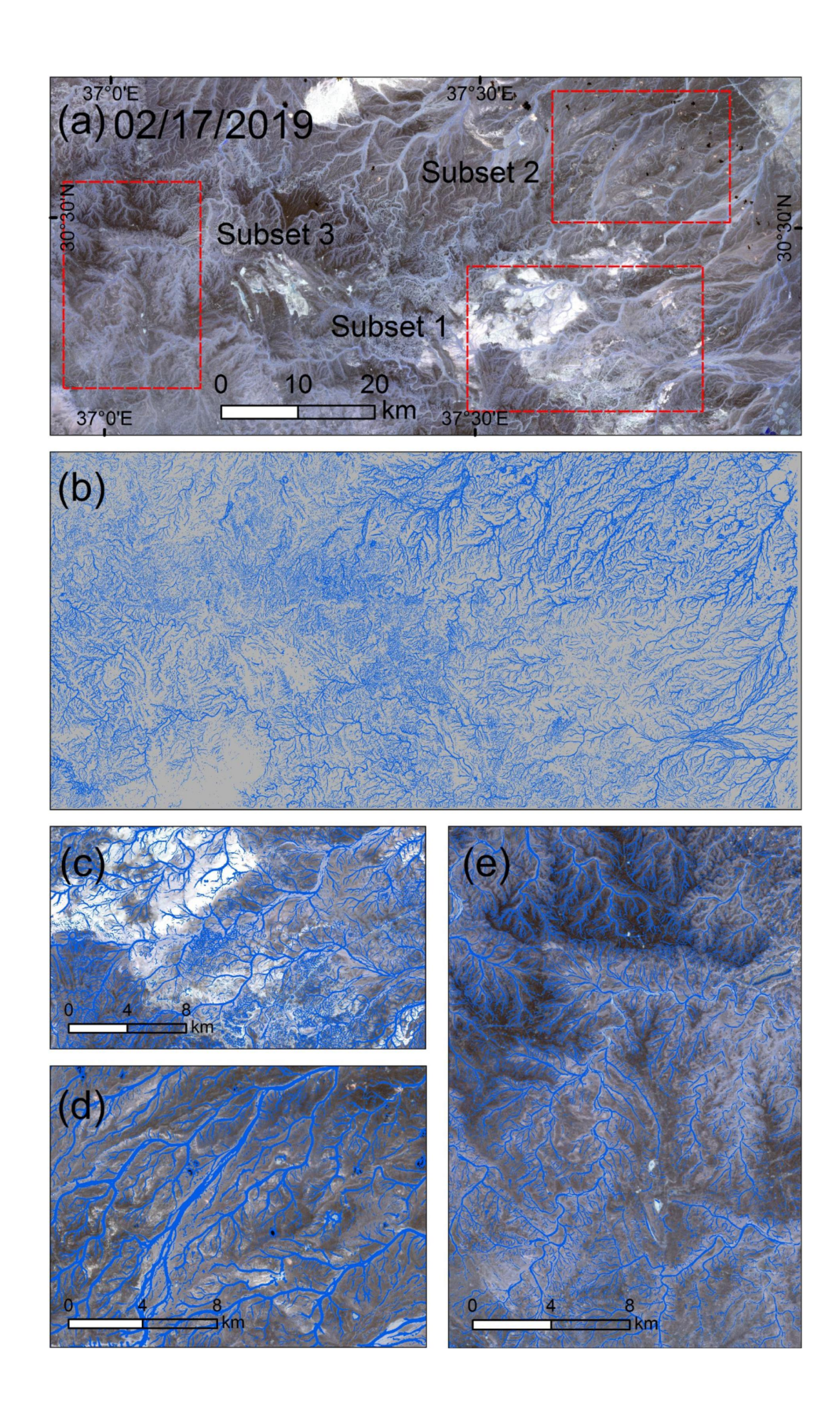


**Fig. 14.** Wadis extraction in Jordan using the AMRGM: (a) color composite image taken on 02/17/2019 (32°14′ N, 37°29′9″ E). (b) Wadis extraction with AMRGM. (c), (d) and (e) represents the complex river networks in Subset 1, Subset 2, and Subset 3 of (a).

Adaptive, multi-scale network growth is the core of the AMRGM, allowing its application to different remote sensing datasets. To some extent, the AMRGM works better in large resolution images where obvious river boundaries are present. We present an application of the method to Landsat images in Fig. 15, where we display the historical changes of the Zagya Zangbo River from 1990 to 2019. Similar to the wadis in the Arabian Peninsula, the Zagya Zangbo is a seasonal river influenced by glacier meltwater and precipitation (Gao et al. 2017; Yao et al. 2012). The discharge and turbidity of the Tibetan Plateau rivers in the cold season is lower than in summer (Song et al. 2014). This study only selects summer images (in August, September, and October) to monitor variations in Zagya Zangbo River's runoff. The turbidity of the Zagya Zangbo River has limited influence on river extraction because of the background homogenization. The Zagya Zangbo River morphology changes little between 1990 and 2000, but the braided streams underwent large-scale reorganization between 2004 and 2011, driven by an increase in seasonal runoff. As a result, more water was discharged by the river into the Siling Lake, changing the lake's area, volume, and turbidity (Mi et al. 2019; Yan and Zheng 2015).

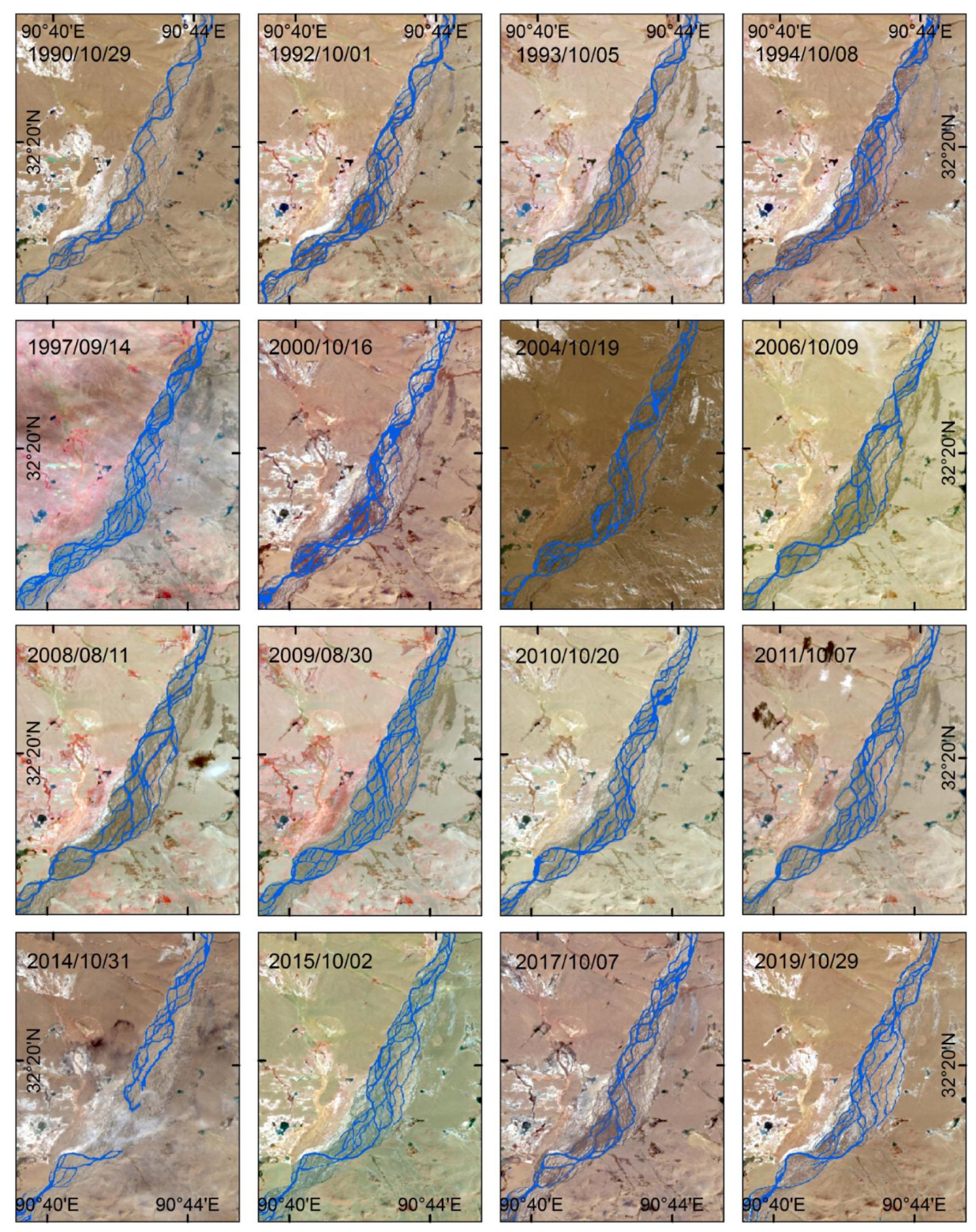


**Fig. 15.** Historical maps of the Zagya Zangbo River (32°20′50″ N, 90°43′08″ E) derived from Landsat images from 1990 to 2019. All images have < 10% clouds and were downloaded from collection-1 USGS (https://earthexplorer.usgs.gov/).

## 5.4 Limits of the proposed method in specific landscapes

In this study, we have developed a framework to distinguish multi-scale river networks. Like most region growth methods, the generation of initial seed points is an indispensable procedure for the delineation of the network. For example, tidal flat channels along the Jiangsu coast of China (Zhang et al. 2020), can elucidate the method's limit (Fig. 16a). The spectral difference between the tidal channels and the sandy flats is minimal; it is therefore difficult to generate good seed points. As a result the AMRGM fails to delineate the tidal channels accurately. The background homogenization can also be influenced by the surrounding environment. When we apply the NDWI in mountain terrains, snow and ice cover may appear as bright features, and the AMRGM can over classify the channel network. This limitation is evident in the Canadian watershed of Fig. 16b (see red circles). To correctly delineate glacier runoff in the rivers, we must first mask snow areas using topographic slope or the normalized difference snow index (NDSI). Finally, in rivers with dense vegetation, such as in the Volga delta, Russia (red circles in Fig. 16c), the network stops growing because the vegetation reduces the brightness of some streams. The AMRGM is designed to extract bright river pixels, so it cannot identify pixels with low contrast. In these situations, we could modify Eq. 10 to select dark pixels with a bright background. However, rivers with these characteristics are relatively rare, and at this stage of algorithm development, we do not feel the need to include this option in the AMRGM.

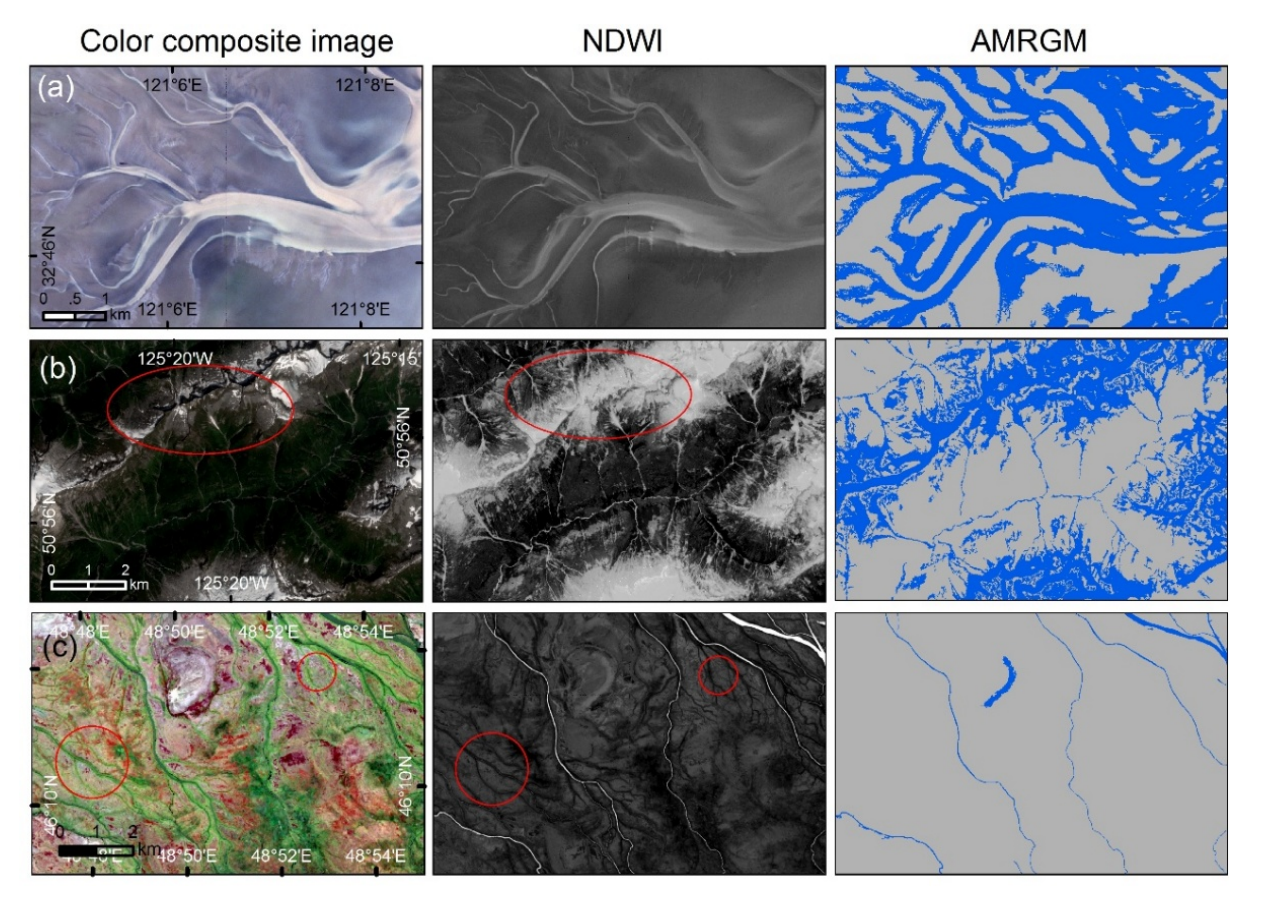


**Fig. 16.** Examples of low performance of the AMRGM: (a) Tidal channels in the radial sand ridges of the Jiang Su coast (02/03/2018). (b) Glacier rivers in snow-covered mountains, Canada (07/08/2019). (c) dense vegetation choking the distributaries of the Volga delta in Russia (04/10/2016).

#### 6. Conclusions

Rivers are sensitive to the effects of global warming and often experience changes in length, width, and drainage density. Open-source moderate-resolution images (e.g., MSI images) provide an opportunity to map river networks at a large scale. Still, accurate river extraction is challenging, especially for delineating river networks with multi-scale morphologies, variable curvatures, and heterogeneous background. Here we propose an algorithm called AMRGM (adaptive and multi-scale region growth method) to delineate multi-scale complex river networks from MSI images.

In the proposed AMRGM, three targeted optimizations are adopted, including a bias-corrected fuzzy C-means (BCFCM) to mitigate background heterogeneity, a scale enhancement based on the Hessian Matrix to make full use of scale and direction information, and a region growth to handle various river sizes. The first two procedures are used to enhance the whole river system, while the latter step is designed to extract multi-scale

river networks. The core of the AMRGM is the multi-scale regional growth criterion, with the addition of river pixel direction to distinguish small and narrow river branches.

A comparison with conventional supervised and unsupervised classification methods indicates that the AMRGM yields superior results in eight test sites around the world. The extraction accuracy for these examples is generally > 0.95, except for sites in England and on the Tibet Plateau, due to their distinctively complex spectral features. Moreover, a time series of Landsat images in a Tibet Plateau river show that our method can also be applied to other remote sensing datasets. During the process of extraction, relevant parameters are set based on trial-and-error analysis for diverse river environments. In our method, thresholds are assigned after analyzing the BCFCM image and are therefore site-specific. An adaptive threshold determination in the AMRGM will be attempted in the future. Although the AMRGM is designed for extracting linear rivers through a multi-scale strategy, it can also be applied to other linear features, such as roads, vegetation, or lake boundaries.

# 627 Appendix

629

### **Table A1.** Summary of acronyms used in the study.

Parameter	Value
I	BCFCM image
В	Binary image
F	Outliers removal image
S	Processing queue
$\sigma$ ; $\sigma_{max}$ , $\sigma_{min}$ , $\sigma_{step}$	Factor scale; maximum, minimum, and step scale
q	Seed point
P	River pixel
Ω	Orientation correlation index
$I_{max}$	Maximum pixel value in a sliding window
M	Test sliding window in large or small scale river
$T_1, T_2$	Outlier removal in a sliding window

Algorithm 1: Multi-scale region growth. Pixel direction is only used for small rivers with low contrast.

```
Data: BCFCM image I
Result: Binary image B
Initialization: \sigma \leftarrow \sigma_{\max}; processing queue S
begin
   while \sigma \ge \sigma_{\min} do
       compute river L_{\sigma} and D_{\sigma} by Eq. 10 and Eq. 14 from I
       while S \neq \emptyset do
            q \leftarrow p \in S
           if \sigma > 3 (For large-scale, middle-scale river)
            for all p \in N_4(q) do
                 if p \notin B and p satisfies Eq. 16 then
                    append p to B and S
              end for
           end if
            if \sigma \le 3 (For small-scale river)
              for all p \in N_8(q) do
                  if p \notin B and p satisfies \Omega_{\sigma}(p,q) > \sqrt{3}/2 then append p to B and S
              end for
           end if
           delete q from S
       end while
   end while
return B
```

632 **Algorithm 2:** Outlier removal.

```
Data: BCFCM image (I), Binary image (B)

Result: Outliers removal image (F)

begin

for all p \in B do

if I_{max} >= M and I_p < T_1 then

delete p in B

end if

else if I_p < T_2 then

delete p in B

end else

end for

F \leftarrow B

return F
```

631

#### Reference

- Abdul Aziz, O.I., Burn, D.H., 2006. Trends and variability in the hydrological regime of the Mackenzie River Basin. *J. Hydrol.* 319, 282–294. https://doi.org/10.1016/j.jhydrol.2005.06.039.
- Acharya, T.D., Subedi, A., Lee, D.H, 2018. Evaluation of Water Indices for Surface Water Extraction in a Landsat 8
   Scene of Nepal. Sensors. 18(8), 2580. https://doi.org/10.3390/s18082580.
- Ahmed, M.N., Yamany, S.M., Mohamed, N., Farag, A.A., Moriarty, T., 2002. A modified fuzzy c-means algorithm
   for bias field estimation and segmentation of MRI data. *IEEE Trans. Med Imaing.* 21, 193–199. https://
   10.1109/42.996338.
- Bezdek, J.C., Ehrlich, R., Full, W., 1984. FCM: The fuzzy c-means clustering algorithm. *Comput Geosci.* 10, 191–203. https://doi.org/10.1016/0098-3004(84)90020-7.
- Bookhagen, B., Burbank, D.W., 2010. Toward a complete Himalayan hydrological budget: Spatiotemporal distribution of snowmelt and rainfall and their impact on river discharge. *J. Geophys. Res.* 115. https://doi.org/10.1029/2009JF001426.
- Briant, R.M., Wainwright, J., Maddy, D., 2018. New approaches to field-model data comparison: Numerical modelling of the last glacial cycle in the Welland catchment, England. *Geomorphology*, 323, 106–122. https://doi.org/10.1016/j.geomorph.2018.09.006.
- Chen, F., Chen, X., Van de Voorde, T., Roberts, D., Jiang, H., Xu, W., 2020a. Open water detection in urban environments using high spatial resolution remote sensing imagery. *Remote Sens. Environ.* 242, 11706. https://doi.org/10.1016/j.rse.2020.111706.
- Chen, H., Liang, Q., Liang, Z., Liu, Y., Ren, T., 2020b. Extraction of connected river networks from multi-temporal
   remote sensing imagery using a path tracking technique. *Remote Sens. Environ.* 246, 111868.
   https://doi.org/10.1016/j.rse.2020.111868.
- Drusch, M., Del Bello, U., Carlier, S., Colin, O., Fernandez, V., Gascon, F., Hoersch, B., Isola, C., Laberinti, P.,
   Martimort, P., Meygret, A., Spoto, F., Sy, O., Marchese, F., Bargellini, P., 2012. Sentinel-2: ESA's Optical High Resolution Mission for GMES Operational Services. *Remote Sens. Environ.* 120, 25–36.
   https://doi.org/10.1016/j.rse.2011.11.026.
- Du, Y., Zhang, Y., Ling, F., Wang, Q., Li, W., Li, X., 2016. Water Bodies' Mapping from Sentinel-2 Imagery with
   Modified Normalized Difference Water Index at 10-m Spatial Resolution Produced by Sharpening the SWIR
   Band. Remote Sens. 8(4), 354. https://doi.org/10.3390/rs8040354.
- Fagherazzi, S., 2008. Self-organization of tidal deltas. *Proceedings of the National Academy of Sciences*. 105, 18692.
   https://doi.org/10.1073/pnas.0806668105.
- Farinosi, F., Arias, M.E., Lee, E., Longo, M., Pereira, F.F., Livino, A., Moorcroft, P.R., Briscoe, J., 2019. Future
   Climate and Land Use Change Impacts on River Flows in the Tapajós Basin in the Brazilian Amazon. *Earth's Future*. 7, 993–1017. https://doi.org/10.1029/2019EF001198.
- Frangi, A.F., Niessen, W.J., Vincken, K.L., Viergever, M.A., 1998. Multiscale vessel enhancement filtering. In: Wells
   W.M., Colchester A., Delp S. (eds) Medical Image Computing and Computer-Assisted Intervention—
   MICCAI'98. MICCAI 1998. Lecture Notes in Computer Science, vol 1496. Springer, Berlin, Heidelberg.
   https://doi.org/10.1007/BFb0056195.
- Gao, B-c.,1996. NDWI—A normalized difference water index for remote sensing of vegetation liquid water from space. *Remote Sens. Environ.* 58, 257–266. https://doi.org/10.1016/S0034-4257(96)00067–3
- Gao, Z., Niu, F., Wang, Y., Luo, J., Lin, Z., 2017. Impact of a thermokarst lake on the soil hydrological properties in
   permafrost regions of the Qinghai-Tibet Plateau, China. Sci. Total Environ. 574, 751–759.
   https://doi.org/10.1016/j.scitotenv.2016.09.108.

- 677 Ghaffarian, S., Ghaffarian, S., 2014. Automatic histogram-based fuzzy C-means clustering for remote sensing imagery.ISPRS J. Photogramm. *Remote Sens.* 97, 46–57. https://doi.org/10.1016/j.isprsjprs.2014.08.006.
- 679 Grainger, S., Conway, D., 2014. Climate change and International River Boundaries: fixed points in shifting sands.

  WIRES Climate Change. 5, 835–848. https://doi.org/10.1002/wcc.306.
- 681 Griffiths, P., Nendel, C., Hostert, P., 2019. Intra-annual reflectance composites from Sentinel-2 and Landsat for 682 national-scale crop and land cover mapping. Remote Sens. Environ. 220, 135-151. 683 https://doi.org/10.1016/j.rse.2018.10.031.
- Hanbay, K., Talu, M.F., 2018. A novel active contour model for medical images via the Hessian matrix and eigenvalues. *Comput. Math. with Appl.* 75, 3081–3104. https://doi.org/10.1016/j.camwa.2018.01.033.
- Harvey, C.F., Swartz, C.H., Badruzzaman, A.B.M., Keon-Blute, N., Yu, W., Ali, M.A., Jay, J., Beckie, R., Niedan,
   V., Brabander, D., Oates, P.M., Ashfaque, K.N., Islam, S., Hemond, H.F., Ahmed, M.F., 2005. Groundwater
   arsenic contamination on the Ganges Delta: biogeochemistry, hydrology, human perturbations, and human
   suffering on a large scale. *CR. GEOSCI*. 337,285–296. https://doi.org/10.1016/j.crte.2004.10.015.
- Hooshyar, M., Kim, S., Wang, D., Medeiros, S.C. 2015. Wet channel network extraction by integrating LiDAR intensity and elevation data. Water Resour. Res. 51, 10029–10046. https://doi.org/10.1002/2015WR018021.
- Hou, J., van Dijk, A.I.J.M., Renzullo, L.J., Vertessy, R.A., 2018. Using modelled discharge to develop satellite-based
   river gauging: a case study for the Amazon Basin. *Hydrol. Earth Syst. Sci.* 22, 6435–6448.
   https://doi.org/10.5194/hess-22-6435-2018.
- Huang, C., Chen, Y., Zhang, S., Wu, J., 2018. Detecting, Extracting, and Monitoring Surface Water From Space Using
   Optical Sensors: A Review. *Rev. Geophys.* 56, 333–360. https://doi.org/10.1029/2018RG000598.
- Isikdogan, F., Bovik, A., & Passalacqua, P., 2017. RivaMap: An automated river analysis and mapping engine. *Remote Sens. Environ.* 202, 88–97. https://doi.org/10.1016/j.rse.2017.03.044.
- Jia, K., Jiang, W., Li, J., & Tang, Z., 2018. Spectral matching based on discrete particle swarm optimization: A new
   method for terrestrial water body extraction using multi-temporal Landsat 8 images. *Remote Sens. Environ.* 209,
   1–18. https://doi.org/10.1016/j.rse.2018.02.012.
- Jiang, H., Feng, M., Zhu, Y., Lu, N., Huang, J., Xiao, T., 2014. An Automated Method for Extracting Rivers and Lakes from Landsat Imagery. *Remote Sens.* 6, 5067–5089. https://doi.org/10.3390/rs6065067.
- Jiang, W., He, G., Long, T., Ni, Y., Liu, H., Peng, Y., Lv, K., Wang, G., 2018. Multilayer Perceptron Neural Network for Surface Water Extraction in Landsat 8 OLI Satellite Images. *Remote Sens.* 10(5), 755. https://doi.org/10.3390/rs10050755.
- Kaplan, G., Avdan, U., 2017. Object-based water body extraction model using Sentinel-2 satellite imagery Eur. J.
   Remote. Sens. 50, 137–143. https://doi.org/10.1080/22797254.2017.1297540
- 709 Kerkeni, A., Benabdallah, A., Manzanera, A., Bedoui, M.H., 2016. A coronary artery segmentation method based on 710 multiscale analysis and region growing. Comput. Med **Imaging** Graph, 48, 49-61. 711 https://doi.org/10.1016/j.compmedimag.2015.12.004.
- Kersten, P.R., Jong-Sen, L., & Ainsworth, T.L., 2005. Unsupervised classification of polarimetric synthetic aperture
   Radar images using fuzzy clustering and EM clustering. *IEEE Trans. Geosci. Remote Sens.* 43, 519–527.
   https://doi.org/10.1109/TGRS.2004.842108.
- Klemenjak, S., Waske, B., Valero, S., Chanussot, J., 2012. Automatic detection of rivers in high-resolution SAR data.
   *IEEE J-STARS*. 5, 1364–1372. https://doi.org/10.1109/JSTARS.2012.2189099
- 717 Kuenzer, C., Heimhuber, V., Huth, J., Dech, S., 2019. Remote Sensing for the Quantification of Land Surface 718 Dynamics in Large River Delta Regions—A Review. Remote Sens. 11(7),1985. 719 https://doi.org/10.3390/rs11171985.
- Lakemond, R., Sridharan, S., Fookes, C., 2011. Hessian-Based Affine Adaptation of Salient Local Image Features. *J. Math Imaging*. Vis, 44, 150–167. https://doi.org/0.1007/s10851-011-0317-8

- Langat, P.K., Kumar, L., Koech, R., 2019. Monitoring river channel dynamics using remote sensing and GIS techniques. *Geomorphology*. 325, 92–102. https://doi.org/10.1016/j.geomorph.2018.10.007.
- Lara, D.S.D., Faria, A.W.C., Araújo, A.d.A., & Menotti, D. (2009). A Semi-Automatic Method for Segmentation of
   the Coronary Artery Tree from Angiography. In, 2009 XXII Brazilian Symposium on Computer Graphics and
   Image Processing (pp. 194-201)
- Liu, Y., Chen, X., Yang, Y., Sun, C., Zhang, S., 2016. Automated Extraction and Mapping for Desert Wadis from
   Landsat Imagery in Arid West Asia. *Remote Sens*. 8(3), 246. https://doi.org/10.3390/rs8030246
- Liu, Y., Zhou, M., Zhao, S., Zhan, W., Yang, K., Li, M., 2015. Automated extraction of tidal creeks from airborne laser altimetry data. *J. Hydrol.* 527, 1006–1020. https://doi.org/10.1016/j.jhydrol.2015.05.058
- Malladi, R., Sethian, J.A., 1995. Image processing via level set curvature flow. *Proceedings of the National Academy of Sciences of the United States of America*, 92, 7046–7050. https://doi.org/10.1073/pnas.92.15.7046.
- Manniesing, R., Viergever, M.A., Niessen, W.J., 2006. Vessel enhancing diffusion: A scale space representation of vessel structures. *Med Image Anal*, 10, 815–825. https://doi.org/10.1016/j.media.2006.06.003
- McFeeters, S.K.,1996. The use of the Normalized Difference Water Index (NDWI) in the delineation of open water features. *Int. J. Remote Sens*, 17, 1425–1432. https://doi.org/10.1080/01431169608948714.
- 737 Mi, H., Fagherazzi, S., Qiao, G., Hong, Y., Fichot, C.G., 2019. Climate change leads to a doubling of turbidity in a 738 rapidly expanding Tibetan lake. *Sci. Total Environ*. 688, 952–959. 739 https://doi.org/10.1016/j.scitotenv.2019.06.339.
- Nardini, A., Yepez, S., Zuniga, L., Gualtieri, C., Bejarano, M.D., 2020. A Computer Aided Approach for River Styles—Inspired Characterization of Large Basins: The Magdalena River (Colombia). Water, 12(4), 1147. https://doi.org/10.3390/w12041147.
- Nones, M., 2020. Remote sensing and GIS techniques to monitor morphological changes along the middle-lower Vistula River, Poland. *Journal of Applied Water Engineering and Research* 0:0, 1–7 https://doi.org/10.1080/15715124.2020.1742137.
- Olabarriaga, S.D., Breeuwer, M., Niessen, W.J., 2003. Evaluation of Hessian-based filters to enhance the axis of coronary arteries in CT images. *International Congress Series*. 1256, 1191–1196. https://doi.org/10.1016/S0531-5131(03)00307-8.
- Pekel, J.-F., Cottam, A., Gorelick, N., Belward, A.S., 2016. High-resolution mapping of global surface water and its long-term changes. *Nature*. 540, 418–422. https://doi.org/10.1038/nature20584.
- Pekel, J.F., Vancutsem, C., Bastin, L., Clerici, M., Vanbogaert, E., Bartholomé, E., Defourny, P., 2014. A near real-time water surface detection method based on HSV transformation of MODIS multi-spectral time series data.
   *Remote Sens. Environ.* 140, 704–716. https://doi.org/10.1016/j.rse.2013.10.008.
- Plater, A.J., Dugdale, R.E., Ivanovich, M., 1994. Sediment yield determination using uranium-series radionuclides: the case of The Wash and Fenland drainage basin, eastern England. *Geomorphology*. 11, 41–56. https://doi.org/10.1016/0169-555X(94)90041-8.
- Pletterbauer F., Melcher A., Graf W., 2018 Climate Change Impacts in Riverine Ecosystems. In: Schmutz S.,
   Sendzimir J. (eds) Riverine Ecosystem Management. Aquatic Ecology Series, vol 8. Springer, Cham.
   https://doi.org/10.1007/978-3-319-73250-3\_11.
- Rinaldi, M., Gurnell, A.M., del Tánago, M.G., Bussettini, M., Hendriks, D., 2016. Classification of river morphology
   and hydrology to support management and restoration. *Aquat Sci.* 78, 17–33. https://doi.org/10.1007/s00027-015-0438-z.
- Rishikeshan, C.A., Ramesh, H. 2018. An automated mathematical morphology driven algorithm for water body extraction from remotely sensed images. *ISPRS J. Photogramm. Remote Sens.* 146, 11–21. https://doi.org/10.1016/j.isprsjprs.2018.08.014.

- Rosgen, D.L., 1994. A classification of natural rivers. CATENA. 22, 169–199. https://doi.org/10.1016/0341-8162(94)90001-9.
- Sekiguchi, H., Sugimoto, N., Eiho, S., Hanakawa, T., Urayama, S. 2005. Blood vessel segmentation for head MRA
   using branch-based region growing. Syst. Comput. Japan. 36, 80–88. https://doi.org/10.1002/scj.20166.
- Song, C., Huang, B., Richards, K., Ke, L., Hien Phan, V., 2014. Accelerated lake expansion on the Tibetan Plateau in
   the 2000s: Induced by glacial melting or other processes? *Water Resour. Res.* 50, 3170–3186. https://doi.org/10.1002/2013WR014724.
- Spada, D., Molinari, P., Bertoldi, W., Vitti, A., Zolezzi, G. 2018. Multi-Temporal Image Analysis for Fluvial
   Morphological Characterization with Application to Albanian Rivers. ISPRS int. j. geo-inf. 7(8), 314.
   https://doi.org/10.3390/ijgi7080314.
- Thanh-Nho, N., Marchand, C., Strady, E., Huu-Phat, N., Nhu-Trang, T.-T., 2019. Bioaccumulation of some trace
   elements in tropical mangrove plants and snails (Can Gio, Vietnam). *Environ. Pollut.* 248, 635–645.
   https://doi.org/10.1016/j.envpol.2019.02.041.
- Umitsu, M., 1993. Late quaternary sedimentary environments and landforms in the Ganges Delta. *Sedimentary Geology*. 83, 177–186. https://doi.org/10.1016/0037-0738(93)90011-S.
- Vörösmarty, C.J., Meybeck, M., Fekete, B., Sharma, K., Green, P., Syvitski, J.P.M., 2003. Anthropogenic sediment
   retention: major global impact from registered river impoundments. *Glob Planet Change*. 39, 169–190. https://doi.org/10.1016/S0921-8181(03)00023-7.
- Wright, E.E., Hine, A.C., Goodbred, S.L., Locker, S.D.,2005. The Effect of Sea-Level and Climate Change on the
   Development of a Mixed Siliciclastic-Carbonate, Deltaic Coastline: Suwannee River, Florida, U.S.A. *J. SEDIMEN. RES.* 75, 621–635. https://doi.org/10.2110/jsr.2005.051.
- Xu, H., 2007. Modification of normalised difference water index (NDWI) to enhance open water features in remotely sensed imagery. Int. J. Remote Sens.27, 3025–3033. https://doi.org/10.1080/01431160600589179.
- Yan, L., Zheng, M., 2015. Influence of climate change on saline lakes of the Tibet Plateau, 1973–2010. Geomorphology. 246, 68–78. https://doi.org/10.1016/j.geomorph.2015.06.006.
- Yang, K., Li, M., Liu, Y., Cheng, L., Duan, Y., Zhou, M.,2014. River Delineation from Remotely Sensed Imagery
   Using a Multi-Scale Classification Approach. I IEEE J-STARS. 7, 4726–4737.
   https://doi.org/10.1109/JSTARS.2014.2309707.
- Yang, Y., Liu, Y., Zhou, M., Zhang, S., Zhan, W., Sun, C., Duan, Y.,2015. Landsat 8 OLI image based terrestrial
   water extraction from heterogeneous backgrounds using a reflectance homogenization approach. *Remote Sens. Environ.* 171, 14–32. https://doi.org/10.1016/j.rse.2015.10.005.
- Yao, T., Thompson, L., Yang, W., Yu, W., Gao, Y., Guo, X., Yang, X., Duan, K., Zhao, H., Xu, B., Pu, J., Lu, A.,
   Xiang, Y., Kattel, D.B., Joswiak, D., 2012. Different glacier status with atmospheric circulations in Tibetan
   Plateau and surroundings. *Nat. Clim Chang.* 2, 663–667. https://doi.org/10.1038/nclimate1580.
- Zhang, W., Zhang, X., Huang, H., Wang, Y. and Fagherazzi, S., 2020. On the morphology of radial sand ridges. *Earth Surface Processes and Landforms*, 45(11), pp.2613-2630.
- Zhou, Y., Dong, J., Xiao, X., Xiao, T., Yang, Z., Zhao, G., Zou, Z.,Qin, Y., 2017. Open Surface Water Mapping Algorithms: A Comparison of Water-Related Spectral Indices and Sensors. *Water*. 9, 256. https://doi.org/10.3390/w9040256.
- Zhu, C., Zou, B., Zhao, R., Cui, J., Duan, X., Chen, Z., Liang, Y., 2017. Retinal vessel segmentation in colour fundus images using Extreme Learning Machine. *Comput. Med Imaging. Graph.* 55, 68–77. https://doi.org/10.1016/j.compmedimag.2016.05.004.
- Zúquete, S.T., Coelho, J., Rosa, F., Vaz, Y., Cassamá, B., Padre, L., Santos, D., Basto, A.P., Leitão, A., 2017. Tick
   (Acari: Ixodidae) infestations in cattle along Geba River basin in Guinea-Bissau. *Ticks Tick Borne Dis.* 8(7),
   161–169. https://doi.org/10.1016/j.ttbdis.2016.10.013.

Acknowledgement: This study was supported by the National Natural Science Foundation of China (grant number 41971378, 41771471, 42011530088, 41901121), the Jiangsu Provincial Natural Science Foundation (grant number BK20160023), the Natural Science Research Project of Anhui Province (grant number KJ2019A0866), the Program B for Outstanding Ph.D. candidate of Nanjing University, the China Scholarship Council (grant number 201806190197), the Open Fund of the Key Laboratory Coastal Zone Exploitation and Protection, Ministry of Natural Resources of China (Grant No. 2019CZEPK03). SF was partly funded by the USA National Science Foundation awards 1832221 (VCR LTER), 1637630 (PIE LTER). We thank the ESA, NASA, for providing Sentinel-2A/B, Landsat Series.

## 820 **LIST OF TABLES**

- **Table 1.** Test sites characteristic and dataset from Sentinel 2A/2B. Climate type refer to Koeppen Climate System
- **Table 2.** A quantitative index used in the assessment.

#### LIST OF FIGURE CAPTIONS

- 824 Fig. 1. Study area: (a) Map of the study sites; (b) Mackenzie River in the Northwest Territories, Canada; (c) Suwannee
- River in Florida, USA; (d) Amazon River in the State of Pará, Brazil; (e) River Welland in England; (f) Geba River
- in the Quinara Region, Guinea-Bissau; (g) Ganges Delta in Bangladesh; (h) Can Gio Mangrove forest in Vietnam; (i)
- 827 Zagya Zangbo River in Tibet, China.
- 828 Fig. 2. The procedure of the AMRGM, from river enhancement, seed points generation, multi-scale region growth,
- and outlier removal.

- Fig. 3. Background homogenization: (a) NDWI image. (b) Histogram of the NDWI image. (c) BCFCM image. (d)
- Histogram of the BCFCM image.
- 832 Fig. 4. Adaptive multi-scale local differential geometry enhances fluvial features in the River Welland, UK: (a–d)
- results with factor scale  $\sigma = 1, 3, 5$ , and 7, used in enhancing water bodies. Line 1, 2, and 3 cross small, mid, and
- large channels, respectively. Algorithm results in Line 1, 2, and 3 for each scale. The red dotted lines are river
- boundaries; the river response L is normalized in [0, 1].
- 836 Fig. 5. River network direction information: (a) direction computed with the multi-scale algorithm using the local
- 837 differential structure, pixel directions are consistent at the confluence between river branches and the main trunk. Note
- that only a fraction of pixel directions are displayed for clarity. (b), (c) and (d) represent the pixel directions in Subset
- 839 1, Subset 2, and Subset 3.
- Fig. 6. Process of region growth in the River Welland network: (a) Initial seed points (blue pixels) automatically
- generated from the BCFCM image and with some few points added in small rivers. (b-e) River pixels (green pixels)
- expanding from large scale channels to small scale channels. (f) Outlier removal result.
- 843 Fig. 7. Extraction of the network in the River Welland using the AMRGM: (a) Color composite image (R: Band 8,
- G: Band 3; B: Band 2); (b) Accuracy analysis obtained by comparing with the ground truth image. Red pixels represent
- commission errors, while green pixels are omission errors.
- Fig. 8. Comparison of river networks extracted with the AMRGM and SVM from remote sensing images with small
- basin areas: (a1) color composite image of the Suwannee River; (a2, a3, a5) Suwannee River network, Subset 1, and
- 848 Subset 2 river extraction using AMRGM; (a4, a6) Subset 1 and Subset 2 river extraction using SVM; (b1) color
- composite image of the Amazon River; (b2, b3, b5) Amazon River network. Subset 1, and Subset 2 river extraction
- using AMRGM, (b4, b6) Subset 1 and Subset 2 river extraction using SVM; (c1) color composite image of the Can
- 851 Gio Mangrove forest, (c2, c3, c5) Can Gio Mangrove forest networks, Subset 1, and Subset 2 river extraction using
- 852 AMRGM, (c4, c6) Subset 1 and Subset 2 river extraction using SVM; (d1) color composite image of the Zagya Zangbo
- River, (d2, d3, d5) Zagya Zangbo network, Subset 1, and Subset 2 river extraction using AMRGM, (d4, d6) Subset 1
- and Subset 2 river extraction using SVM.
- 855 Fig. 9. Comparison of river networks extracted with the AMRGM and SVM from remote sensing images with a large
- basin area: (a1) color composite image of the Mackenzie River, (a2, a3, a5) Mackenzie River network, Subset 1 and
- 857 Subset 2 river extraction using AMRGM, (a4, a6) Subset 1 and Subset 2 river extraction using SVM; (b1) color
- composite image of the Geba River; (b2, b3, b5) Geba River network, Subset 1 and Subset 2 river extraction using
- AMRGM, (b4, b6) Subset 1 and Subset 2 river extraction using SVM; (c1) color composite image of the Ganges Delta,

- 860 (c2, c3, c5) Ganges Delta network, Subset 1 and Subset 2 river extraction using AMRGM, (c4, c6) Subset 1 and Subset
- 2 river extraction using SVM.
- Fig. 10. The overall performance of AMRGM compared to four other methods: SVM, ML, ISODATA, and KM. (a)-
- 863 (d) overall accuracy, Kappa coefficient, commission, and omission errors for the eight sites. The orange line represents
- the median, and the green dotted line is the mean value.
- **Fig. 11.** Percent increase in identified river pixels as a function of change in scale  $\sigma$ .
- Fig. 12. River delineations from Sentinel-2A MSI images using the AMRGM and compared with HR images, over
- River Welland (UK) and Suwannee River (USA): (a1) The AMRGM delineations from a 10 m MSI image; (a2) Visual
- interpretations from a 1 m HR image (rivers-HR); (a3) The AMRGM delineations and rivers-HR. The grey thin strips
- are rivers-HR that unsuccessfully extracted by the AMRGM. Insets of (a4-1-a11-1) are zoom-in MSI images of these
- un-extract river sections, whereas (a4-2-a11-2) are zoom-in HR images. (b1) The AMRGM delineations from a 10 m
- MSI image; (b2) Visual interpretations from a 1 m HR image (rivers-HR); (b3) The AMRGM delineations and rivers-
- HR. The grey thin strips are rivers-HR that unsuccessfully extracted by the AMRGM. Insets of (b4-1-b11-1) are
- zoom-in MSI images of these un-extract river sections, whereas (b4-2-b11-2) are zoom-in HR images.
- Fig. 13. River number in HR images (Visual interpretation) and Sentinel-2 MSI images (AMRGM). (a) River number
- section of River Welland, England. (b) River number section of Suwannee River, USA. Note that "active channels"
- are counted in HR-image as seldom river spectral exist in the HR-image from the Google Earth.
- Fig. 14. Wadis extraction in Jordan using the AMRGM: (a) color composite image 02/17/2019 (32°14′ N, 37°29′9″
- E). (b) Wadis extraction with AMRGM. (c), (d) and (e) represents the complex river networks in Subset 1, Subset 2,
- and Subset 3 of (a).

- Fig. 15. Historical maps of the Zagya Zangbo River (32°20′50″ N, 90°43′08″ E) derived from Landsat image from
- 881 1990 to 2019. All images have < 10% clouds and were downloaded from collection-1 USGS
- 882 (https://earthexplorer.usgs.gov/).
- 883 Fig. 16. Examples of low performance of the AMRGM: (a) Tidal channels in the radial sand ridges of the Jiang Su
- coast (02/03/2018). (b) Glacier rivers in snow-covered mountains, Canada (07/08/2019). (c) dense vegetation choking
- the distributaries of the Volga delta in Russia (04/10/2016).